Ore Geology Reviews 139 (2021) 104494

Contents lists available at ScienceDirect

Ore Geology Reviews

journal homepage: www.elsevier.com/locate/oregeorev

Cu-Mo infertile granite: Insights from the late cretaceous plutons in the Northern Yidun Terrane, eastern Tibetan Plateau

Li-Chuan Pan [a], Rui-Zhong Hu [a,b,*], Xin-Song Wang [a], Xian-Wu Bi [a], Jing-Jing Zhu [a], Shan-ling Fu [a], Jun Yan [a], Yong Wang [c]

[a] State Key Laboratory of Ore Deposit Geochemistry, Institute of Geochemistry, Chinese Academy of Sciences, Guiyang 550081, China
[b] College of Earth and Planetary Sciences, University of Chinese Academy of Sciences, Beijing 100049, China
[c] The Bureau of Geology and 108 Mineral Exploration Team of Sichuan Province, Chengdu 611200, China

ARTICLE INFO

Keywords:
Yidun Terrane granite
Magma fertility
Porphyry Cu ± Mo deposit
Oxidation state
Sr–Nd isotope

ABSTRACT

The Yidun Cu-Mo polymetallic metallogenic belt, located in the eastern Tibetan Plateau, is well known for numerous Mesozoic porphyry Cu–Mo deposits. The Cu-Mo deposits are only concentrated in the southern part of the belt while the granites situated in the north are generally barren in Cu-Mo mineralization. To understand the cause of Cu and Mo infertility, geochronology and petro-mineral geochemistry of three Cu- and Mo-barren granite plutons (Cilincuo, Rongyicuo, and Hagela) in the Northern Yidun Terrane were investigated. Petro-geochemical characteristics and zircon U-Pb dating (95–85 Ma) along with the tectonic evolution history confirmed that the three plutons formed in a Late Cretaceous intracontinental setting. The whole-rock geochemical compositions showed that these plutons can be classified as A-type granites and have undergone extensive magmatic differentiation. Based on the calculated magmatic oxygen fugacity using zircon composition and a set of geochemical criteria including whole-rock Sr/Y ratios, Eu/Eu* and Fe^{3+}/Fe^{2+} values as well as apatite Cl-H_2O contents, the parental magma of the Cilincuo pluton was identified as more oxidized and H_2O-Cl-rich than those of the Rongyicuo and Hagela plutons. These features enable the Cilincuo pluton to have an elevated capacity of Cu mineralization compared to the other two plutons. However, the causative magmas of the three plutons are still not enough hydrous and oxidized for typical porphyry Cu ± Mo mineralization. The whole-rock Sr-Nd isotope values of these three plutons are consistent with Late Triassic Cu and Mo barren granites in the same region such as Dongcuo, Cuojiaoma and Sucuoma, suggesting that they were derived from a similar magma source which might lack the oxidized and hydrous Neoproterozoic arc root remnant.

1. Introduction

Porphyry Cu ± Mo deposits are the most important repository of these metals in the world (Cook et al., 2005; Sillitoe, 2010). This type of deposit mainly occurs in active continental margins, where the partial melting of the overlying mantle wedge due to water addition via ocean slab subduction produces hydrous-oxidized magmas that trigger porphyry Cu ± Mo mineralization (Richards, 2003, 2009; Cook et al., 2005; Sillitoe, 2010). Recently, porphyry Cu ± Mo deposits have been recognized to occur in tectonic settings that have no active subductions (Hou et al., 2004a; 2009; 2015; Wang et al., 2018a). Despite the controversy regarding the genesis of post-collisional porphyry Cu ± Mo deposits including the sources of porphyry magma and ore-forming materials (Wang et al., 2014a; Hou et al., 2004b; 2009; 2013a; 2015; 2017), it has gradually been accepted that a hydrous and oxidized magma system is required for the porphyry Cu and Mo mineralization occurring in the post-collisional setting (Hou et al., 2020). Abundant H_2O can provide sufficient exsolving hydrothermal fluids (Richards and Kerrich, 2007). The oxidized magma can prevent the early saturation of Cu- and Mo-bearing sulfides, which ensures sufficient extraction of ore-forming elements by hydrothermal fluids for later mineralization (Candela and Holland, 1984; Richards, 2003, 2015; Rempel et al., 2006; Jugo, 2009; Sun et al., 2013). As a result, the oxidation state and water content of parental magmas have been suggested as crucial indexes for evaluating the Cu ± Mo mineralization potential of porphyries whether these porphyries are formed in the subduction setting or in the post-collisional setting (e.g., Richards, 2009, Wang et al., 2014a; Yang et al., 2017).

The Yidun Terrane is an important Cu and Mo polymetallic metallogenic belt in southwestern China (Li et al., 2014), in which numerous Mesozoic granites outcrop from the north to the south of the belt. These

* Corresponding author at: State Key Laboratory of Ore Deposit Geochemistry, Institute of Geochemistry, Chinese Academy of Sciences, Guiyang 550081, China.

https://doi.org/10.1016/j.oregeorev.2021.104494
Received 14 May 2021; Received in revised form 15 July 2021; Accepted 19 September 2021
Available online 23 September 2021

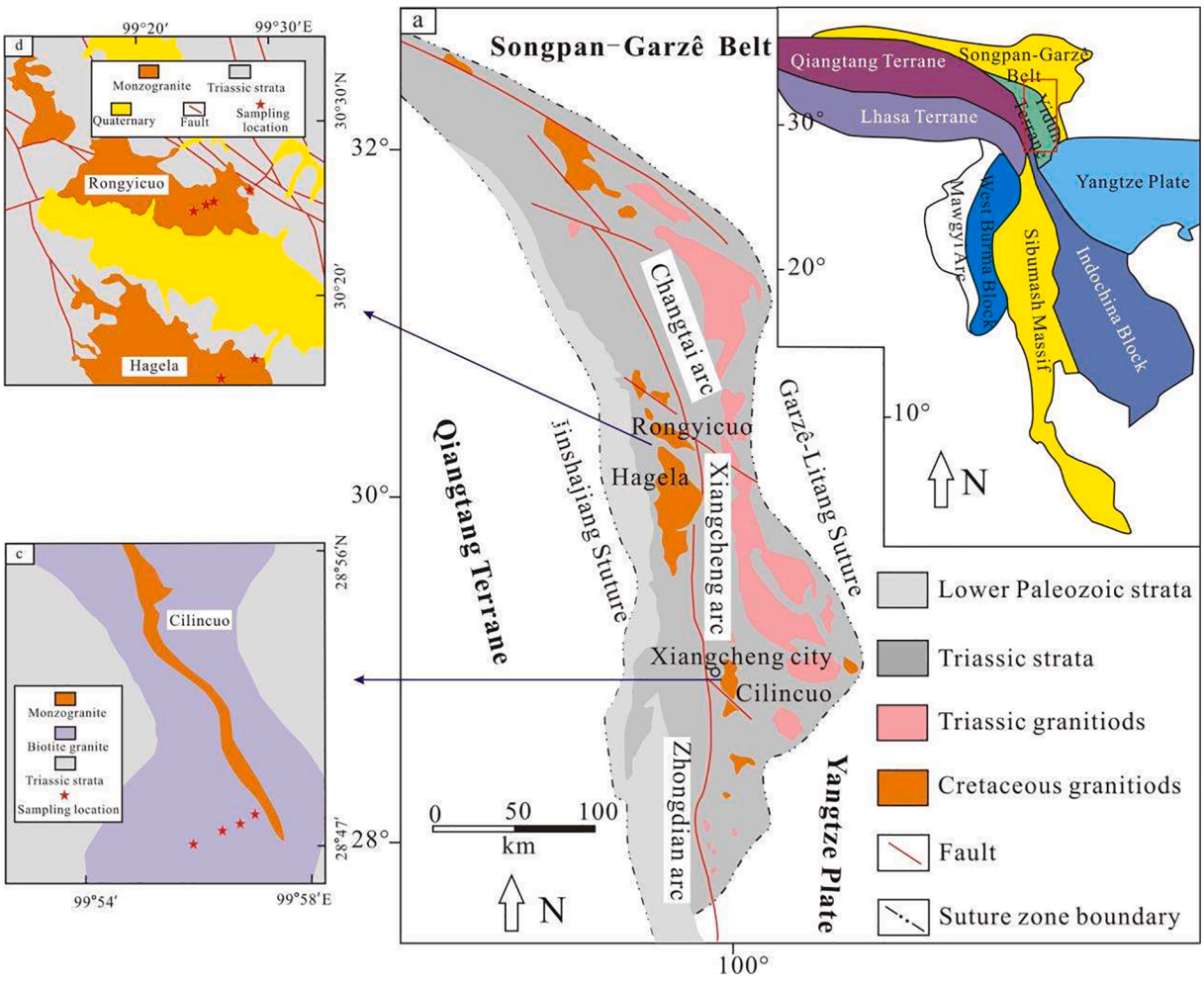

Fig. 1. Regional geological map of the studied area (a) and simplified geological maps of the Cilincuo (b), Rongyicuo, and Hagela plutons (c).

granite plutons have similar mineral assemblages and chemical compositions but have distinctly different capacities of Cu ± Mo mineralization. In particular, these plutons in the southern Yidun Terrane contain numerous porphyry Cu ± Mo deposits (Wang et al., 2014b; 2014c; Li et al., 2017; He et al., 2019), whereas those in the northern part are generally barren in Cu and Mo mineralization (Yang et al., 2020). Many studies have been carried out on the the Cu ± Mo mineralization of granites in the Yidun Terrane, and found these ore-forming granite plutons have high magmatic fertility (e.g., He et al., 2019; Gao et al., 2020). But less attention has been paid to the Cu- and Mo-barren plutons. The reasons for the difference in the Cu ± Mo mineralization capacity of granites that are closely related in time and space are still unclear. The magma oxidation states and water contents of the Cu- and Mo-barren plutons are also not well understood.

To address these questions, we selected three representative Cu- and Mo-barren granitic plutons (Cilincuo, Rongyicuo, and Hagela) in the Northern Yidun Terrane to carry out an integrated study of geochronology and petro-mineral geochemistry. First, a detailed investigation of zircon U–Pb dating of the selected plutons is reported. Furthermore, magma oxidation states, H_2O-Cl abundances, and magma sources of these three plutons are also evaluated using the geochemical data of zircon, apatite, and their host rocks. Finally, based on the magma information, we explain the cause of the Cu-Mo infertility of these granitic plutons investigated.

2. Geologic setting

The NW-trending Yidun Terrane extends for ~ 500 km long and lies alone the Qiangtang block, the Songpan–Garzê block and the Yangtze Craton (Fig. 1**a**). It is defined by the Garzê-Litang Suture to the east and the Jinshajiang Suture to the west (Fig. 1**b**). The Garzê-Litang Ocean, a branch of the Paleo-Tethys Ocean, opened in the Late Permian which may be triggered by a plume beneath the western margin of the Yangtze Craton (Song et al., 2004; Xiao et al., 2008), or the eastward subduction of the Jinshajiang oceanic slab (Roger et al., 2008; 2010). The opening of the Garzê-Litang Ocean segregated the Zhongdian-Zhongza massif from the Yangtze Craton (Hou et al., 2003). In Late Triassic, the westward Garzê-Litang oceanic slab subduction caused the formation of the Yidun Terrane in the east of the Zhongdian-Zhongza massif (Hou et al., 2004c; 2007; Deng et al., 2014). The Yidun Terrane that is covered by Middle and Late Triassic volcanic-sedimentary successions can be subdivided into the Changtai and Xiangcheng arcs in the north, and the Zhongdian arc in the south (Hou et al., 2007; Li et al., 2011). At the end of the Triassic, the Yidun Terrane collided with the Songpan-Garzê block, resulting in Indosinian magmatism and Cu-Mo mineralization (Hou et al., 2003). After the Garzê-Litang Ocean closure, the regional textural setting was transferred into an intracontinental deformation stage. In the Late Cretaceous, a series of post-collisional granitic plutons emplaced into the Yidun Terrane, with some forming porphyry Cu ± Mo deposits such as Hongshan, Relin, and Tongchanggou in the southern Yidun Terrane (Qu et al., 2002; Wang et al., 2014b, 2014c; Yang et al., 2015; Gao et al., 2017). The more northerly coeval granite plutons,

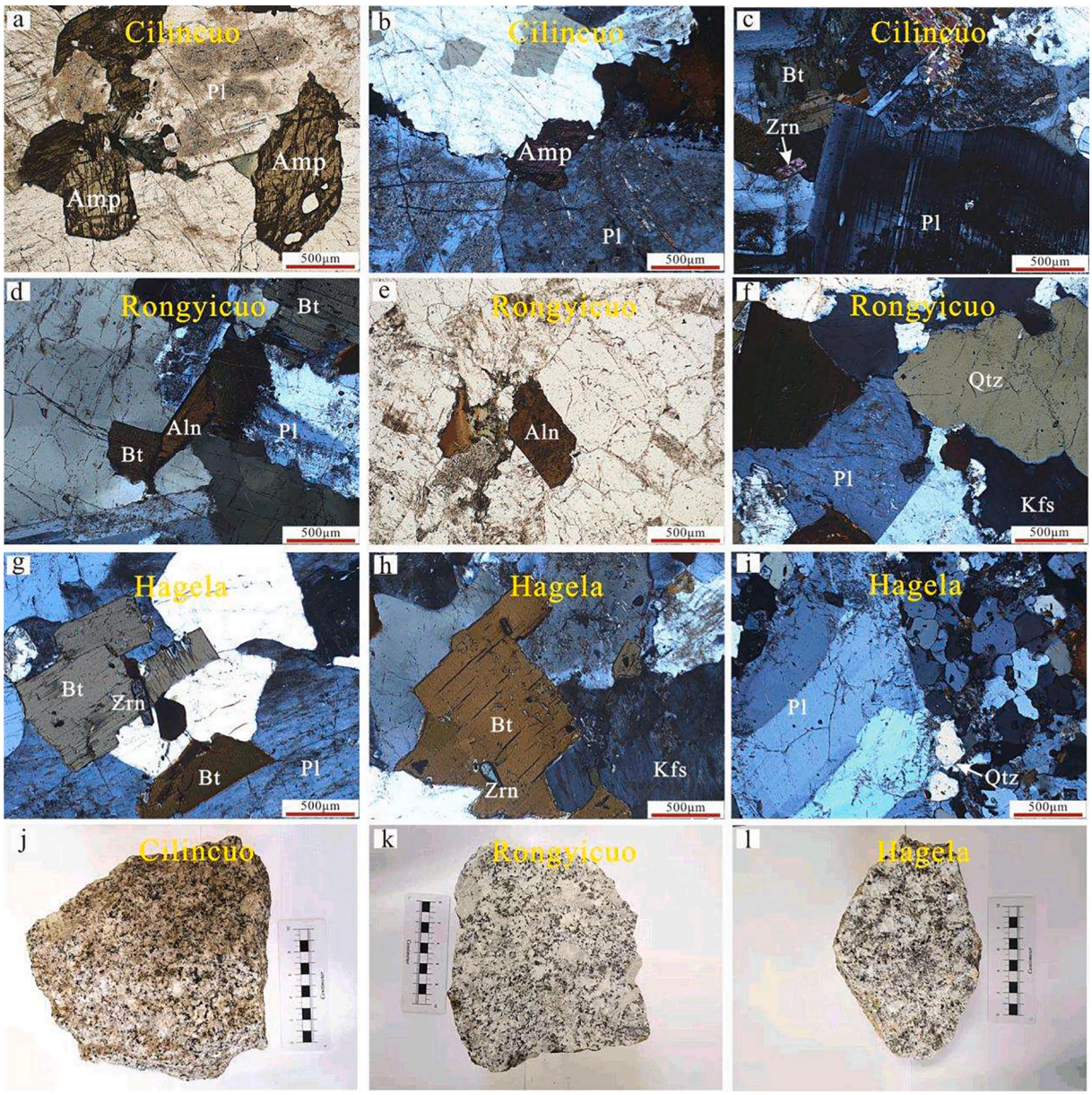

Fig. 2. Photomicrographs and hand specimens of the Cilincuo (a–c, j), Rongyicuo (d–f, k), and Hagela (g–i, l) plutons in the Yidun Terrane . Aln: allanite; Bt: biotite; Kfs: K-feldspar; Qtz: quartz, Pl: plagioclase; Amp: amphibole; Zrn: zircon.

however, do not contain any significant porphyry Cu and Mo deposits, although they may have potential genetic links to some Sn-Ag-Pb-Zn polymetallic deposits. The representative examples of Cu ± Mo infertile plutons in this region are such as Cilincuo, Rongyicuo, and Hagela.

The Cilincuo pluton is located about 10 km southeast of the Xiangcheng County. This pluton is distributed in a NS-trending direction intruding into the Late Triassic sandstone, siltstone and silty slate. This pluton consists of biotite granite and a small volume of fine-grained monzogranite (Fig. 1**c**). The dominant biotite granite mainly consists of K-feldspar (~30%), plagioclase (~20%), quartz (~25%), biotite (~15%), and amphibole (~10%) **(**Fig. 2**a–c**). The accessory minerals include apatite, titanite, and zircon. The sparse Cu mineralization occurs in monzogranite accompanied by hydrothermal alteration including silicification, chloritization, epidotization, sericitization, and kaolinization. But there is no obvious hydrothermal Cu mineralization in biotite granite. Geochronology has shown that this pluton may form at 65–60 Ma (Lu and Wang, 1993) or 79.3 Ma (Fei et al., 2015).

The Cu- and Mo-barren Rongyicuo and Hagela plutons are all located to the north of the Cilincuo pluton (Fig. 1**d**). The Rongyicuo pluton covering 122 km^2, trends in an approximately east–west direction and intrudes into the Late Triassic carbonate and clastic rock. The Rongyicuo pluton is predominantly composed of monzogranite that contains quartz (~30%), plagioclase (~30%), K-feldspar (~35%), and biotite (~5%) as major phases, and apatite, allanite, and zircon as accessory phases (Fig. 2**d–f**). Some dioritic enclaves can be observed in this pluton, and are interpreted as a result of magmatic contamination during diagenesis (Yin 2018). The Hagela pluton lies about 15 km to the south of the Rongyicuo pluton. This pluton intrudes into the Late Triassic carbonate and clastic rock, covering an area of approximately 440 km^2. The Hagela pluton is dominated by monzogranite that mainly composed of plagioclase (35%), K-feldspar (30%), quartz (25%), and biotite (10%). The accessory minerals mainly include apatite and zircon (Fig. 2**g–i**). The zircon U-Pb and biotite ^{40}Ar-^{39}Ar dating of the Rongyicuo and Hagela plutons yield crystallization ages of 100–90 Ma (Reid et al., 2005; Yang et al., 2020). Considering limitation in analytical techniques and relatively excessive error between different methods, more geochronology

Table 1
Sample information of the Cilincuo, Rongyicuo and Hagela plutons.

Pluton	Sample ID	Rock type	Sampling location	Whole-rock analysis	Mineral selection (apatite and zircon)
Cilincuo	CLC-1	Biotite granite	28° 47′ 42″99° 56′ 03″	√	√
	CLC-2		28° 47′	√	
	CLC-3		48″99° 56′ 53″	√	
	CLC-4		28° 47′ 38″99° 56′ 37″	√	
	CLC-5		28° 48′ 07″99° 57′ 27″	√	
Rongyicuo	RYC-1	Monzogranite	30° 25′ 59″99° 29′ 28″	√	√
	RYC-2		30° 25′ 47″99° 26′ 30″	√	
	RYC-3		30° 25′	√	
	RYC-4		14″99° 25′ 43″	√	
	RYC-5		30° 24′ 38″99° 23′ 44″	√	
Hagela	HGL-1	Monzogranite	30° 17′	√	√
	HGL-2		07″99° 29′	√	
	HGL-3		25″	√	
	HGL-4		30° 15′	√	
	HGL-5		64″99° 26′ 19″	√	

data are needed to precisely define the formation age of these plutons. It is noteworthy that although these two plutons cannot generate any important Cu and Mo mineralization, there are some Sn-Ag-Pb-Zn polymetallic deposits around them, such as Xiasai. This deposit containing 1028 t Ag and 0.27 Mt Pb + Zn is considered as a hydrothermal Ag-Pb-Zn deposit and has a potential genetic link with the Rongyicuo pluton (Li et al., 2020; Yang et al., 2020).

3. Sampling and analytical methods

3.1. Sampling methods

We selected fifteen fresh rock samples for chemical analysis. Among them, five biotite granite samples were from the Cilincuo pluton and ten monzogranite samples were from the Rongyicuo and Hagela plutons. One rock sample of each pluton was selected to separate apatite and zircon crystals for chemical analysis. Sample details including sampling location are listed in Table 1.

3.2. Whole-rock major and trace element analysis

The whole-rock samples used in this study were relatively fresh. The major element concentrations in the selected rocks were determined with fused lithium tetraborate glass pellets using an Axios PW4400 X-ray fluorescence spectrometer at the State Key Laboratory of Ore Deposit Geochemistry, Institute of Geochemistry, Chinese Academy of Sciences in Guiyang (SKLODG). The analytical precision was estimated to be less than 5%. Trace element concentrations in the whole rocks were analyzed using a PE DRC-e ICP-MS at SKLODG. Powdered samples (50 mg) were dissolved in a mixture of HF and HNO_3 in high-pressure polytetrafluoroethylene vessels for 2 days at ~ 190 °C. Rh was used to monitor signal drift during the analysis. The detailed analytical procedures were described by Qi et al. (2000). The analytical precision was estimated to be within 10%.

3.3. Whole-rock Sr and Nd isotopic analysis

Whole-rock Sr–Nd isotope analyses were performed using a Neptune Plus MC-ICP-MS at SKLODG. For Sr–Nd isotope analyses, the analytical protocols followed those of Yang et al. (2007) and Zhou et al. (2020). Briefly, sample powders (~100 mg) were dissolved in distilled HF–HNO_3 solutions in Savillex screw top Teflon beakers at 150 °C. Then, the Sr and REE fractions were separated on columns filled with the AG50W-X8 resin. Finally, the separation of Nd from the REE fractions was performed on Ln-spec resin columns. The measured Sr and Nd isotopic ratios were normalized using the exponential law, with $^{86}Sr/^{88}Sr$ reference values of 0.1194 and $^{146}Nd/^{144}Nd$ reference values of 0.7219, respectively. Analyses of standards NIST SRM 987 and Jndi-1 over the measurement session yielded $^{87}Sr/^{86}Sr = 0.710261 \pm 12$ (2sd, n = 5) and $^{143}Nd/^{144}Nd = 0.512084 \pm 11$ (2sd, n = 5), respectively.

3.4. Apatite major elements compositions analysis

Apatite crystals were separated from the rocks using standard heavy-liquid and magnetic methods. Subsequently, the crystals were mounted and polished using an epoxy resin. Cathodoluminescence images were used to choose appropriate targets for in situ analysis. The major and minor element apatite contents were determined using a JEOL-1600 electron microprobe at SKLODG. The analytical conditions were as follows: accelerating voltage of 25 kV, beam current of 10nA, and beam diameter of 10 μm. The following natural minerals were used for calibration: apatite (P, S, F), kaersutite (Ca, Mn, Na, Al, Si, Fe), and tugtupite (Cl).

3.5. Zircon U–Pb ages and trace elements analysis

Zircon U–Pb dating was analyzed by LA-ICP-MS at SKLODG, using an Agilent 7900 ICP-MS equipped with a GeoLasPro 193 nm ArF excimer laser. A laser repetition of 6 Hz, energy density of 3 J/cm^2, and spot size of 32 μm were used for this analysis. The 91,500 standard was used as the external isotopic calibration standard and was analyzed twice every 8–10 analyses. Plešovice and Qinghu zircons were used for quality control and obtained consistent ages of 336.9 ± 2.9 Ma (N = 6) and 159.7 ± 1.4 Ma (N = 6), respectively. More details are provided in Tang et al. (2020). The zircon trace element concentrations were measured under the same experimental conditions. The NIST610 and NIST612 standards were used for calibration. Offline data reduction was then performed using the ICPMSDataCal software from Liu et al. (2008).

3.6. Zircon Hf isotopic analysis

Zircon Hf isotopes were analyzed at Nanjing FocuMS Technology Co. Ltd. using a Teledyne Cetac Technologies Analyte Excite laser ablation system and Nu Instruments Nu Plasma II MC-ICP-MS. A 193 nm ArF excimer laser, which was homogenized by a set of beam delivery systems, was focused on the zircon surface with a fluence of 6.0 J/cm^2. The ablation was conducted with a spot diameter of 50 μm at a repetition rate of 8 Hz for 40 s (equating to 320 pulses). Helium was used as the carrier gas to ensure the efficient transport of the resulting aerosol to the MC-ICP-MS. Two of the following zircon standards, Qinghu, GJ-1, 91500, Plešovice, Penglai, and MudTank, were analyzed after every ten unknown samples to provide quality control. Additional details of the operating conditions and analytical methods can be found in Liu et al. (2017).

Table 2
The results of major (wt.%) and trace elements (ppm) analyzes for the Cilincuo, Rongyicuo and Hagela plutons.

Plutons	Cilincuo pluton (biotite granite)					Rongyicuo pluton (monzogranite)					Hagela pluton (monzogranite)				
Sample number	CLC-1	CLC-2	CLC-3	CLC-4	CLC-5	RYC-1	RYC-2	RYC-3	RYC-4	RYC-5	HGL-1	HGL-2	HGL-3	HGL-4	HGL-5
SiO2	68.60	69.21	69.14	68.40	69.94	75.90	74.12	72.73	72.22	71.78	69.29	68.33	69.11	73.12	71.60
Al2O3	14.44	14.51	14.75	14.32	14.76	12.54	13.02	13.95	13.96	13.26	13.98	14.67	14.46	12.94	13.57
TFe2O3	3.00	3.57	3.44	3.55	2.65	1.32	1.98	2.17	2.16	3.34	4.15	4.34	4.09	2.96	2.99
MgO	0.77	1.01	0.97	1.10	0.65	0.15	0.42	0.47	0.47	0.94	1.00	1.12	1.03	0.68	0.64
CaO	1.98	2.13	2.21	2.50	1.36	0.84	1.28	1.62	1.62	2.10	1.80	1.81	1.86	1.60	1.68
Na2O	3.74	3.70	3.84	3.61	4.06	3.21	3.23	3.15	3.17	3.07	2.80	2.83	2.82	2.81	2.90
K2O	4.75	4.53	4.40	4.30	4.50	4.94	4.69	4.83	4.76	4.14	4.58	4.89	4.87	4.45	4.90
P2O5	0.17	0.21	0.21	0.22	0.16	0.03	0.08	0.08	0.09	0.17	0.17	0.16	0.17	0.12	0.13
TiO2	0.45	0.55	0.53	0.55	0.42	0.11	0.27	0.33	0.34	0.55	0.59	0.61	0.59	0.45	0.46
MnO	0.05	0.06	0.06	0.06	0.03	0.03	0.05	0.06	0.06	0.07	0.05	0.05	0.05	0.06	0.05
L.O.I. 1000	1.43	0.32	0.43	0.48	0.65	0.35	0.31	0.51	0.62	0.49	0.87	0.67	0.93	0.63	0.41
Total	99.38	99.80	99.98	99.09	99.18	99.42	99.45	99.90	99.47	99.91	99.28	99.48	99.98	99.82	99.33
Na2O + K2O	8.49	8.23	8.24	7.91	8.56	8.15	7.92	7.98	7.93	7.21	7.38	7.72	7.69	7.26	7.80
K2O/Na2O	1.27	1.22	1.15	1.19	1.11	1.54	1.45	1.53	1.50	1.35	1.64	1.73	1.73	1.58	1.69
A/CNK	0.97	0.97	0.98	0.94	1.05	1.03	1.02	1.04	1.05	0.99	1.09	1.11	1.09	1.05	1.03
Fe3+/Fe2+	0.17	0.21	0.22	0.13	0.26	0.03	0.05	0.05	0.13	0.19	0.12	0.12	0.14	0.13	0.10
Rittmann index	3.05	2.80	2.81	2.67	2.94	2.15	2.15	2.30	2.31	1.94	2.24	2.55	2.45	1.87	2.29
Ga	22.5	22.8	22.9	22.0	22.0	18.3	20.4	21.4	21.3	20.0	23.3	22.8	24.0	21.9	22.1
Rb	197	212	197	199	218	277	262	256	253	220	265	253	274	253	238
Ba	920	791	805	724	800	90	272	748	820	396	674	807	838	506	654
Sr	369	361	383	376	312	57	128	226	232	223	226	236	264	195	223
Zr	237	268	223	249	228	96	164	186	204	267	278	255	254	236	236
Nb	39.5	46.6	46.0	41.8	41.5	24.8	29.4	27.7	27.8	31.0	30.9	30.6	31.7	28.6	28.5
Hf	6.48	7.12	5.99	6.49	5.66	3.58	5.41	5.18	5.62	7.44	7.49	7.17	6.40	6.47	6.26
Ta	3.78	4.68	4.75	4.92	3.98	4.48	6.05	4.28	4.35	4.75	3.41	3.44	3.51	3.64	3.54
Th	48.9	47.7	43.5	41.2	46.6	37.9	38.1	32.8	34.3	38.5	31.9	28.0	30.7	39.5	38.0
U	9.27	10.0	9.00	9.98	11.4	15.8	16.5	8.64	11.9	15.6	9.51	7.28	10.7	11.9	13.3
La	85.9	73.1	74.0	73.2	74.6	27.9	38.8	45.7	51.2	51.4	54.5	52.1	53.6	63.9	53.5
Ce	154	127	133	136	134	56.8	77.4	82.6	90.2	99.3	116	110	107	123	104
Pr	16.9	14.4	14.6	14.8	14.4	6.6	8.4	8.8	9.9	11.2	12.2	12.0	11.9	14.2	11.8
Nd	50.5	45.7	46.6	50.1	44.4	25.2	32.1	32.2	35.6	40.0	43.7	42.2	39.8	45.4	41.7
Sm	8.37	8.28	8.14	8.69	8.26	6.72	7.11	6.21	6.54	7.31	8.22	8.42	8.28	9.10	8.78
Eu	1.18	1.27	1.23	1.23	1.12	0.26	0.55	0.83	0.75	0.93	1.01	1.08	1.16	0.91	1.05
Gd	5.91	6.57	6.24	6.91	5.45	6.46	6.46	4.81	5.62	6.50	7.05	6.40	6.86	6.62	6.44
Tb	0.97	1.03	1.03	1.01	0.92	1.11	1.13	0.76	0.87	0.95	1.16	1.16	1.16	1.09	1.13
Dy	4.85	5.82	5.76	5.55	4.53	7.49	6.74	4.32	5.03	5.40	6.76	6.19	6.26	6.52	6.56
Ho	1.00	1.18	1.14	1.10	0.93	1.53	1.59	0.97	1.10	1.25	1.28	1.25	1.38	1.20	1.33
Er	2.69	3.52	3.28	3.11	2.81	4.43	4.15	2.45	2.93	3.40	3.76	3.42	3.87	3.55	3.63
Tm	0.41	0.51	0.47	0.49	0.43	0.68	0.73	0.38	0.48	0.54	0.54	0.50	0.57	0.56	0.59
Yb	2.80	3.78	3.36	3.21	2.63	4.82	5.34	2.86	3.27	3.62	3.72	3.48	3.72	3.80	3.49
Lu	0.44	0.50	0.48	0.53	0.41	0.73	0.75	0.42	0.45	0.56	0.54	0.49	0.51	0.55	0.53
Y	28.7	33.7	31.4	31.8	27.6	45.9	44.2	27.5	32.0	34.4	36.2	34.9	37.3	35.9	36.8
Pb	29.9	28.1	26.9	27.0	24.8	37.1	44.1	37.5	37.0	29.3	32.7	34.9	36.1	24.3	28.5
∑REE	336	293	299	306	295	151	191	193	214	232	260	249	246	281	245
Sr/Y	12.9	10.7	12.2	11.8	11.3	1.2	2.9	8.2	7.2	6.5	6.3	6.7	7.1	5.4	6.1
(La/Yb)N	22.0	13.9	15.8	16.3	20.4	4.2	5.2	11.4	11.3	10.2	10.5	10.7	10.3	12.1	11.0
(La/Sm)N	6.6	5.7	5.9	5.4	5.8	2.7	3.5	4.7	5.1	4.5	4.3	4.0	4.2	4.5	3.9
(Sm/Yb)N	3.3	2.4	2.7	3.0	3.5	1.5	1.5	2.4	2.2	2.2	2.5	2.7	2.5	2.7	2.8
δEu	0.51	0.53	0.53	0.49	0.51	0.12	0.25	0.46	0.38	0.41	0.40	0.45	0.47	0.36	0.43
δCe	0.99	0.96	0.99	1.01	1.00	1.03	1.05	1.01	0.98	1.01	1.10	1.08	1.04	1.01	1.02

Rittmann index= (Na2O + K2O)2/(SiO2 − 43), δEu = EuN/(SmN × GdN)(1/2), δCe = CeN/(LaN × PrN)(1/2)

4. Results

4.1. Whole-rock major and trace compositions

The major and trace elemental compositions of the rock samples from the three selected plutons are listed in Table 2. The data therein show that the three plutons are calc-alkaline (Rittmann index of 1.87–3.05) and metaluminous–peraluminous (aluminum saturation index of 0.94–1.11) (see Fig. 3**a, b**). The samples from the Cilincuo pluton have lower SiO_2 (68.40–69.94 wt%) but higher CaO contents (0.36–2.50 wt%) than other two plutons. The samples from the Rongyicuo pluton have SiO_2 contents from 71.78 to 75.90 wt% and CaO contents from 0.84 to 2.10 wt%; the samples from the Hagela pluton have SiO_2 contents from 68.33 to 73.21 wt% and CaO from 0.60 to 1.86 wt%. The whole-rock MgO, Fe_2O_3, Al_2O_3, P_2O_5, and TiO_2 contents were similar to those of the Cilincuo pluton (MgO: 0.65–1.10 wt%; Fe_2O_3: 2.96–4.34 wt%; Al_2O_3: 14.32–14.76 wt%; P_2O_5: 0.16–0.22 wt%; TiO_2: 0.42–0.55 wt%) and Hagela plutons (MgO: 0.64–1.12 wt%; Fe_2O_3: 2.65–3.57 wt%; Al_2O_3: 12.94–14.67 wt%; P_2O_5: 0.12–0.17 wt%; TiO_2: 0.45–0.61 wt%). However, these values were higher in the Rongyicuo pluton (MgO: 0.15–0.94 wt%; Fe_2O_3: 1.32–3.34 wt%; Al_2O_3: 12.54–13.96 wt%; P_2O_5: 0.03–0.17 wt%; TiO_2: 0.11–0.55 wt%).

It is apparent that all samples displayed fractionated REE patterns in the chondrite- normalized REE diagram (see Fig. 4**a**). Among the three plutons, the samples from the Cilincuo pluton have the highest $(La/Yb)_N$ values from 13.9 to 22 and Eu/Eu* values from 0.49 to 0.53. The samples from the Hagela pluton have medium $(La/Yb)_N$ values from 10.3 to 12.1 and Eu/Eu* values from 0.36 to 0.47. The Rongyicuo pluton has the lowest $(La/Yb)_N$ value from 4.1 to 12.4, and Eu/Eu* values from 0.13 to 0.46. The chondrite-normalized trace-element patterns of the samples are shown in Fig. 4b. All rock samples were characterized by mild to strong depletion of Ba, Nb, Sr, P, and Ti.

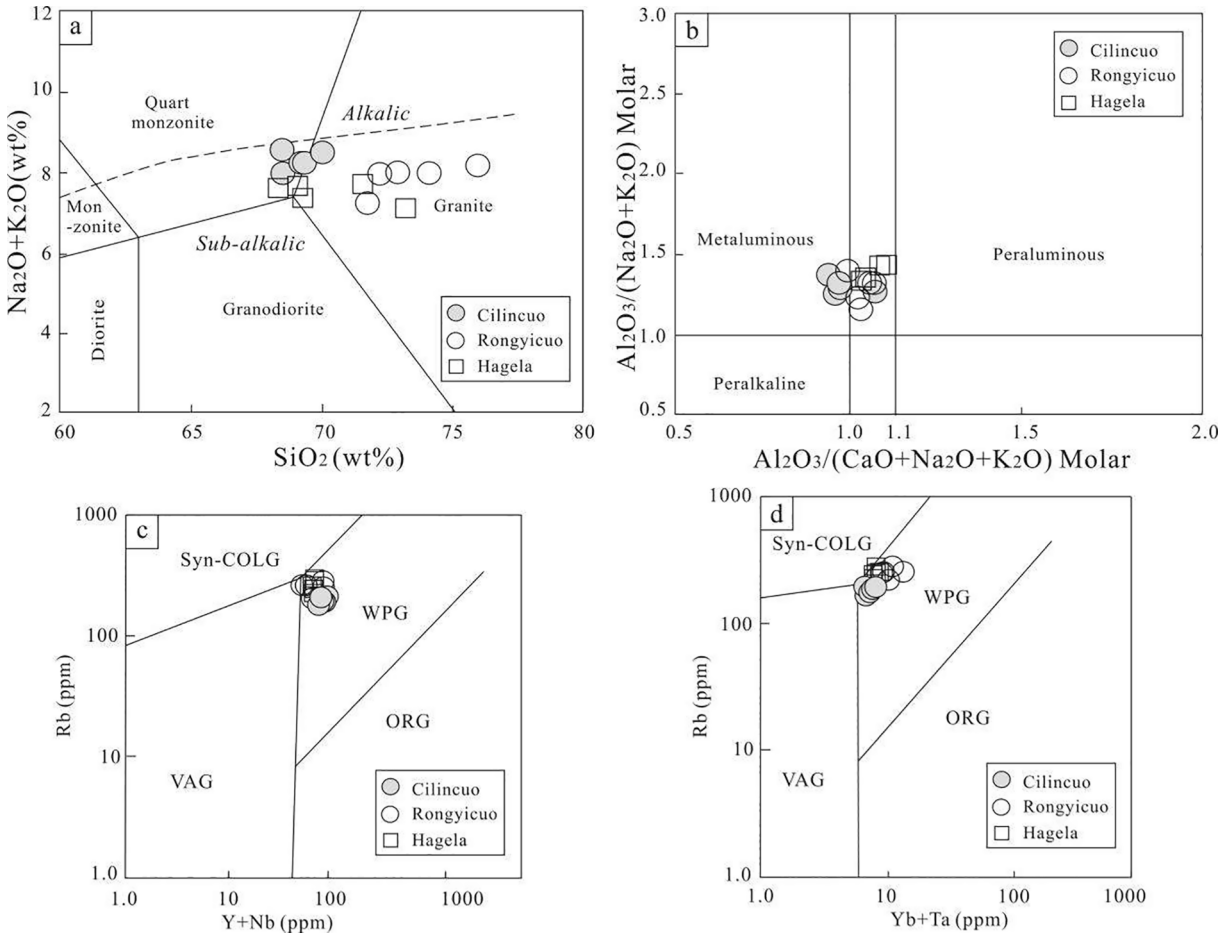

Fig. 3. Total alkali vs. SiO_2 diagram (Middlemost, 1994) (a), A/NK vs. A/CNK diagram (Maniar and Piccoli, 1989) (b), Rb vs. Y + Nb (c) and Rb vs.Yb + Ta (d) discriminant diagram for *syn*-collision (Syn-COL), volcanic arc (VA), within plate (WP) and normal and anomalous ocean ridge (OR) granite (Pearce 1996).

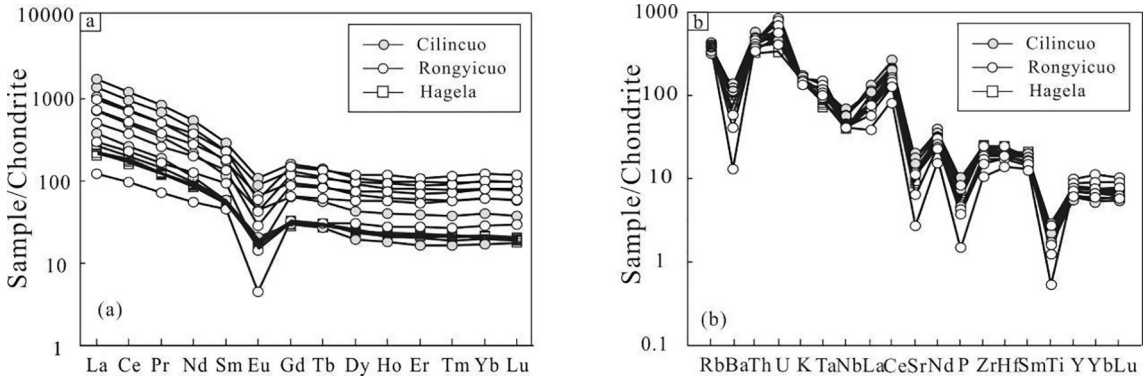

Fig. 4. Chondrite-normalized REE diagrams (a) and trace-element diagrams (b) for the Cilincuo, Rongyicuo, and Hagela plutons.

4.2. Zircon U–Pb ages and trace elements

The zircon U-Pb ages of the three selected plutons are listed in Table 3. The zircon grains from the samples (Cilincuo, Rongyicuo, and Hagela) were colorless and euhedral with igneous oscillatory zoning. Twenty zircon analyses from the Cilincuo pluton yielded $^{206}Pb/^{238}U$ ages varying from 84.3 Ma to 88.9 Ma with a weighted mean $^{206}Pb/^{238}U$ age of 86.1 ± 0.5 Ma (2σ, MSWD = 1.3) (Fig. 5**a**). Twenty-one zircon analyses from the Rongyicuo pluton yielded $^{206}Pb/^{238}U$ ages ranging from 95.5 Ma to 99.5 Ma with a weighted mean age of 98.0 ± 0.5 Ma (2σ, MSWD = 0.9) (Fig. 5**b**). Fifteen zircon analyses from the Hagela pluton yielded $^{206}Pb/^{238}U$ ages ranging from 94.3 Ma to 98.8 Ma with a weighted mean age of 97.1 ± 0.8 Ma (2σ, MSWD = 1.3) (Fig. 5**c**).

The zircon trace element contents are listed in Table 4. The high Th/U ratios (>0.1) suggest that the selected zircon crystals are igneous and has not been subjected to the serious hydrothermal alteration (Möller et al., 2003). The Ce contents of zircon are 2.78–11.52 ppm, 5.43–35.44 ppm, and 5.26–28.04 ppm, the Ti contents of zircon are 2.77–8.78 ppm, 1.13–6.62 ppm and 0.98–10.74 ppm and the U content of zircon are 145–545, 249–2030, and 373–4149 ppm in the Hagela, Cilincuo, and Rongyicuo plutons, respectively. Based on zircon Ti, Ce, and U contents, we calculated the magmatic oxygen fugacity using the method proposed

Table 3
LA–ICP–MS Zircon U–Pb analytical results for the Cilincuo, Rongyicuo and Hagela plutons.

Plutons	Spot No.	Pb (ppm)	Th (ppm)	U (ppm)	Th/U	$^{207}Pb/^{206}Pb$	1σ Err.	$^{207}Pb/^{235}U$	1σ Err.	$^{206}Pb/^{238}U$	1σ Err.	$^{208}Pb/^{232}Th$	1σ Err.	$^{207}Pb/^{235}U$ Age (Ma)	1σ Err.	$^{206}Pb/^{238}U$Age (Ma)	1σ Err.	$^{208}Pb/^{232}Th$Age (Ma)	1σ Err.
Cilincuo	1	13.78	702	791	0.89	0.0491	0.0022	0.0923	0.0040	0.0136	0.0001	0.0042	0.0001	89.6	3.7	86.9	1.0	84.7	1.7
	2	26.11	522	1820	0.29	0.0512	0.0015	0.0937	0.0028	0.0132	0.0001	0.0043	0.0001	91.0	2.6	84.3	0.8	86.8	2.1
	3	18.59	642	1191	0.54	0.0458	0.0017	0.0856	0.0032	0.0134	0.0002	0.0044	0.0001	83.4	3.0	85.9	1.1	87.8	2.1
	4	12.23	475	770	0.62	0.0483	0.0022	0.0904	0.0040	0.0135	0.0002	0.0041	0.0001	87.9	3.8	86.4	1.1	83.3	2.5
	5	25.85	647	1783	0.36	0.0494	0.0014	0.0912	0.0028	0.0133	0.0002	0.0045	0.0001	88.6	2.6	85.0	1.0	89.7	1.9
	6	14.40	388	967	0.40	0.0496	0.0018	0.0917	0.0032	0.0134	0.0002	0.0042	0.0001	89.1	3.0	86.0	1.1	84.7	1.9
	7	12.59	407	817	0.50	0.0488	0.0020	0.0888	0.0032	0.0133	0.0002	0.0042	0.0001	86.4	3.0	85.2	1.0	85.4	1.9
	8	16.10	339	1113	0.30	0.0476	0.0015	0.0876	0.0028	0.0133	0.0001	0.0043	0.0001	85.3	2.6	85.1	0.9	85.8	2.2
	9	13.88	529	871	0.61	0.0499	0.0018	0.0933	0.0032	0.0135	0.0001	0.0042	0.0001	90.6	3.0	86.6	0.9	85.0	1.8
	10	8.81	368	548	0.67	0.0488	0.0020	0.0913	0.0037	0.0135	0.0002	0.0044	0.0001	88.7	3.4	86.6	1.0	88.7	2.3
	11	8.99	296	556	0.53	0.0505	0.0022	0.0967	0.0042	0.0139	0.0002	0.0045	0.0001	93.7	3.9	88.9	1.2	91.4	2.2
	12	6.62	289	418	0.69	0.0527	0.0028	0.0996	0.0051	0.0137	0.0002	0.0043	0.0001	96.4	4.7	87.7	1.3	87.3	2.9
	13	29.52	581	2036	0.29	0.0466	0.0013	0.0863	0.0024	0.0134	0.0001	0.0044	0.0001	84.1	2.2	85.6	0.8	89.6	1.7
	14	28.97	605	1987	0.30	0.0485	0.0015	0.0900	0.0027	0.0134	0.0001	0.0043	0.0001	87.5	2.5	85.7	0.8	87.3	1.9
	15	18.17	586	1152	0.51	0.0500	0.0017	0.0945	0.0032	0.0136	0.0002	0.0045	0.0001	91.7	2.9	87.3	1.0	90.0	2.0
	16	21.10	568	1408	0.40	0.0496	0.0015	0.0929	0.0029	0.0135	0.0002	0.0043	0.0001	90.2	2.7	86.5	1.0	85.9	2.0
	17	8.27	313	542	0.58	0.0461	0.0023	0.0847	0.0041	0.0135	0.0002	0.0041	0.0001	82.6	3.9	86.5	1.3	83.0	2.7
	18	22.62	881	1379	0.64	0.0458	0.0016	0.0871	0.0029	0.0137	0.0001	0.0045	0.0001	84.8	2.8	87.9	0.9	90.4	1.9
	19	14.23	485	922	0.53	0.0469	0.0018	0.0857	0.0031	0.0132	0.0001	0.0041	0.0001	83.5	2.9	84.6	1.0	82.7	1.9
	20	11.02	386	695	0.56	0.0482	0.0022	0.0904	0.0042	0.0136	0.0002	0.0044	0.0001	87.9	3.9	87.0	1.4	88.3	2.7
Rongyicuo	1	28.88	203	1882	0.11	0.0469	0.0012	0.0967	0.0024	0.0149	0.0001	0.0049	0.0001	93.7	2.2	95.5	0.9	99.2	3.0
	2	53.88	1090	3204	0.34	0.0483	0.0012	0.1020	0.0025	0.0152	0.0001	0.0049	0.0001	98.7	2.3	97.4	0.8	97.9	1.7
	3	43.71	594	2733	0.22	0.0476	0.0011	0.1021	0.0026	0.0155	0.0002	0.0049	0.0001	98.7	2.4	98.9	1.2	98.6	2.2
	4	34.65	239	2207	0.11	0.0488	0.0012	0.1023	0.0025	0.0151	0.0001	0.0053	0.0001	98.9	2.3	96.9	0.9	107	2.8
	5	39.15	330	2446	0.13	0.0456	0.0011	0.0971	0.0025	0.0153	0.0002	0.0051	0.0001	94.0	2.3	98.1	1.0	104	2.4
	6	103.0	1205	6233	0.19	0.0497	0.0012	0.1062	0.0027	0.0154	0.0002	0.0055	0.0001	103	2.5	98.5	1.1	111	2.4
	7	48.92	478	3106	0.15	0.0496	0.0012	0.1062	0.0029	0.0154	0.0002	0.0056	0.0002	103	2.6	98.5	1.2	114	3.4
	8	45.40	451	2882	0.16	0.0485	0.0010	0.1030	0.0022	0.0154	0.0002	0.0054	0.0001	99.5	2.0	98.3	1.0	110	2.8
	9	22.24	1022	1177	0.87	0.0488	0.0017	0.1042	0.0037	0.0155	0.0002	0.0048	0.0001	101	3.4	99.1	1.1	97.4	1.6
	10	54.49	579	3468	0.17	0.0463	0.0010	0.0980	0.0019	0.0153	0.0001	0.0051	0.0001	94.9	1.8	98.2	0.8	104	1.9
	11	47.43	522	3080	0.17	0.0487	0.0010	0.1029	0.0021	0.0152	0.0002	0.0051	0.0001	99.4	2.0	97.6	1.0	102	2.3
	12	48.20	525	3085	0.17	0.0501	0.0010	0.1079	0.0025	0.0156	0.0002	0.0053	0.0001	104	2.3	99.5	1.1	107	2.3
	13	11.42	520	602	0.86	0.0490	0.0019	0.1022	0.0039	0.0152	0.0002	0.0048	0.0001	98.8	3.6	97.1	1.3	97.4	2.0
	14	33.09	209	2187	0.10	0.0485	0.0012	0.1037	0.0026	0.0154	0.0002	0.0050	0.0001	100	2.4	98.8	1.0	100	3.0
	15	65.33	801	4162	0.19	0.0463	0.0009	0.0982	0.0021	0.0153	0.0001	0.0050	0.0001	95.1	1.9	98.1	1.0	101	1.8
	16	33.26	391	2157	0.18	0.0462	0.0013	0.0970	0.0027	0.0152	0.0002	0.0051	0.0002	94.0	2.5	97.6	1.2	103	3.1
	17	61.32	528	4095	0.13	0.0480	0.0011	0.1003	0.0025	0.0151	0.0002	0.0049	0.0001	97.1	2.3	96.6	1.2	99.5	2.6
	18	33.26	509	2084	0.24	0.0471	0.0013	0.1003	0.0027	0.0155	0.0002	0.0049	0.0001	97.1	2.5	99.0	1.2	98.8	2.2
	19	45.36	894	2788	0.32	0.0475	0.0011	0.1020	0.0026	0.0155	0.0002	0.0049	0.0001	98.6	2.4	99.2	1.4	99.5	2.1
	20	57.54	560	3673	0.15	0.0490	0.0011	0.1051	0.0026	0.0155	0.0002	0.0050	0.0001	101	2.4	99.1	1.3	101	2.1
	21	66.55	730	4105	0.18	0.0502	0.0010	0.1074	0.0026	0.0154	0.0002	0.0056	0.0002	104	2.3	98.8	1.3	114	3.3
Hagela	1	10.26	253	597	0.42	0.0500	0.0023	0.1070	0.0055	0.0153	0.0002	0.0051	0.0002	103	5.1	98.1	1.5	103	3.3
	2	8.83	238	517	0.46	0.0469	0.0023	0.0968	0.0047	0.0150	0.0002	0.0047	0.0001	93.8	4.3	96.2	1.3	94.1	2.5
	3	25.99	401	1597	0.25	0.0441	0.0015	0.0929	0.0032	0.0152	0.0002	0.0047	0.0001	90.2	2.9	97.3	1.0	94.7	2.5
	4	4.98	123	297	0.41	0.0492	0.0037	0.1032	0.0069	0.0153	0.0003	0.0044	0.0002	99.7	6.3	98.1	1.9	89.1	4.8
	5	2.62	64.1	154	0.42	0.0494	0.0036	0.1009	0.0065	0.0150	0.0003	0.0049	0.0003	97.6	6.0	95.9	1.7	99.6	5.2
	6	9.20	215	514	0.42	0.0518	0.0026	0.1101	0.0055	0.0154	0.0002	0.0052	0.0001	106	5.0	98.8	1.1	104	2.6
	7	32.43	558	1950	0.29	0.0489	0.0014	0.1016	0.0029	0.0150	0.0001	0.0048	0.0001	98.3	2.6	96.1	0.9	97.6	2.1
	8	13.01	266	780	0.34	0.0467	0.0017	0.0988	0.0036	0.0154	0.0002	0.0050	0.0001	95.7	3.3	98.8	1.3	100	3.0
	9	9.85	386	530	0.73	0.0554	0.0026	0.1134	0.0049	0.0149	0.0002	0.0046	0.0001	109	4.5	95.1	1.2	91.9	2.4
	10	10.77	429	578	0.74	0.0498	0.0022	0.1024	0.0044	0.0150	0.0002	0.0046	0.0001	99.0	4.0	96.0	1.2	93.7	2.6
	11	17.27	298	1014	0.29	0.0569	0.0019	0.1210	0.0043	0.0153	0.0002	0.0056	0.0001	116	3.9	98.0	1.2	112	2.9
	12	31.73	433	1891	0.23	0.0576	0.0016	0.1218	0.0031	0.0154	0.0002	0.0065	0.0001	117	2.8	98.3	1.2	131	2.7
	13	4.65	89.0	285	0.31	0.0406	0.0025	0.0863	0.0048	0.0154	0.0002	0.0044	0.0002	84.1	4.5	98.3	1.3	89.4	4.0

(*continued on next page*)

Table 3 (*continued*)

Plutons	Spot No.	Pb (ppm)	Th (ppm)	U (ppm)	Th/ U	$^{207}Pb/^{206}Pb$	1σ Err.	$^{207}Pb/^{235}U$	1σ Err.	$^{206}Pb/^{238}U$	1σ Err.	$^{208}Pb/^{232}Th$	1σ Err.	$^{207}Pb/^{235}U$ Age (Ma)	1σ Err.	$^{206}Pb/^{238}U$Age (Ma)	1σ Err.	$^{208}Pb/^{232}Th$Age (Ma)	1σ Err.
	14	13.33	289	761	0.38	0.0570	0.0020	0.1211	0.0042	0.0154	0.0002	0.0054	0.0001	116	3.8	98.4	1.3	108	2.5
	15	92.3	1210	5628	0.22	0.0611	0.0014	0.1248	0.0031	0.0147	0.0002	0.0066	0.0001	119	2.8	94.3	1.4	132	2.2

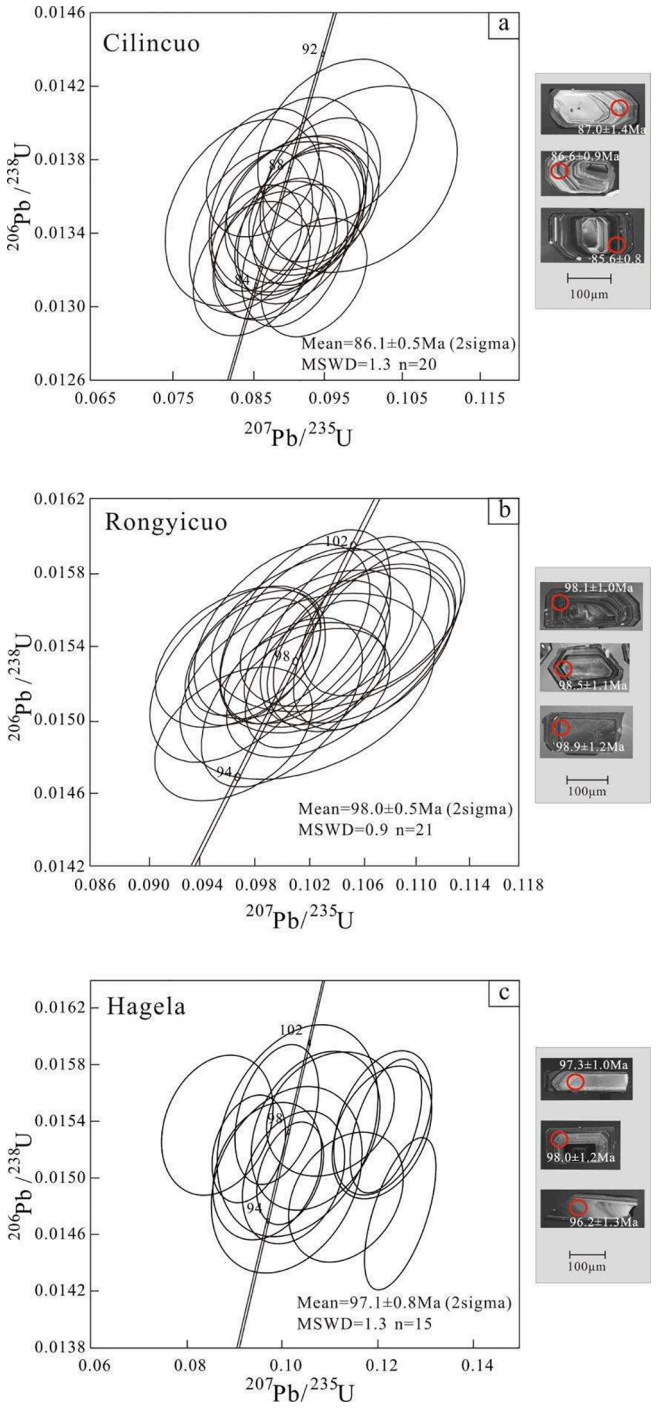

Fig. 5. Zircon U–Pb concordia diagrams of the Cilincuo (a), Rongyicuo (b), and Hagela (c) plutons.

by Loucks et al. (2020). The result revealed that the magma fO_2 values were △FQM − 0.3, △FQM − 0.8, and △FQM − 1.2 in the Cilincuo, Rongyicuo, and Hagela plutons, respectively.

4.3. Zircon Hf isotopes

The zircon Hf isotope results are presented and summarized in Table 5 and Fig. 6. Twenty-nine zircon analyses from the Cilincuo pluton (86.1 Ma) yielded $\varepsilon_{Hf}(t)$ values between − 3.6 and − 1.6 with T_{DM2} model ages of 1.25–1.38 Ga. Twenty-nine analyses of zircons from the Hagela pluton (97.1 Ma) yielded $\varepsilon_{Hf}(t)$ values ranging from − 7.8 to − 3.1 with T_{DM2} model ages of 1.35–1.65 Ga. Twenty-seven zircon

Table 4
Zircon trace elements concentrations and calculated magmatic oxygen fugacity.

Plutons	La	Ce	Pr	Nd	Sm	Eu	Gd	Tb	Dy	Ho	Er	Tm	Yb	Lu	Y	Nb	Hf	Ta	Th	U	Ti	U total	△FMQ	Average △FMQ	St dev
Hagela	0.03	4.65	0.05	0.60	1.85	0.06	10.8	3.77	48.2	19.2	86.8	19.0	176	36.4	532	2.98	12,452	1.66	115	391	4.18	394	−1.5	−1.2	0.7
	0.07	6.70	0.08	1.61	2.84	0.12	18.8	6.01	70.6	26.5	117	24.3	223	45.0	736	4.03	11,017	1.92	203	475	3.76	478	−0.9		
	0.04	4.61	0.07	1.22	2.72	0.16	15.4	4.98	60.3	23.0	98.3	20.4	181	36.1	623	2.63	10,354	1.22	117	265	8.78	267	−1.8		
	0.00	2.78	0.07	1.23	3.02	0.23	14.4	4.84	56.1	21.7	96.0	20.0	182	37.0	596	1.44	9225	0.87	61.2	145	8.76	146	−2.1		
	0.09	6.29	0.12	1.84	3.26	0.17	18.0	6.32	75.7	28.8	127	27.1	240	48.9	788	4.44	11,626	2.02	216	514	5.32	518	−1.4		
	0.02	9.37	0.10	1.36	2.78	0.11	15.0	5.62	69.2	26.3	124	26.4	236	48.5	749	4.10	12,026	2.85	178	539	2.77	543	−0.2		
	0.03	11.5	0.34	5.65	9.37	0.43	42.8	13.5	145	49.8	204	40.1	345	65.2	1344	4.06	12,024	2.07	303	485	4.31	489	−0.1		
	0.23	7.42	0.66	9.34	14.8	1.33	68.1	21.0	219	75.5	305	58.8	497	96.7	1998	3.19	9274	1.38	422	545	8.15	549	−1.5		
	0.02	5.87	0.05	1.04	3.16	0.13	16.7	6.11	71.7	27.6	122	25.8	235	48.1	754	3.47	11,473	1.93	162	467	6.73	470	−1.6		
Cilincuo	0.21	35.4	1.46	19.7	25.1	4.92	94.6	27.8	289	101	419	84.8	738	141	2727	7.59	9156	2.70	811	817	3.92	823	1.5	−0.3	0.9
	0.00	10.8	0.06	1.16	2.94	0.08	18.3	6.88	90.7	37.1	178	40.6	381	80.1	1085	12.0	14,131	7.66	524	1832	1.63	1846	−0.5		
	0.04	8.22	0.27	4.04	6.56	0.66	30.0	9.70	111	41.0	182	37.5	342	69.9	1144	3.66	9193	1.74	341	524	4.63	527	−0.8		
	0.04	5.44	0.09	1.73	3.03	0.47	14.8	5.08	57.0	22.3	101	21.7	203	42.0	628	2.20	8771	1.06	121	249	6.62	250	−1.2		
	0.00	11.5	0.06	1.09	2.82	0.06	18.5	7.47	93.9	38.9	188	41.8	395	81.7	1125	13.7	14,133	9.02	580	2030	1.13	2044	−0.2		
	0.02	16.1	0.52	7.49	11.6	0.33	58.1	19.1	216	80.3	349	71.1	634	125	2213	6.72	11,301	3.45	905	1413	2.07	1424	0.2		
	0.03	7.66	0.36	5.29	8.39	0.49	35.2	11.7	132	48.4	210	43.2	380	77.8	1337	2.70	10,092	1.50	343	541	4.87	545	−1.0		
Rong yicuo	0.10	20.5	0.35	5.86	12.2	0.39	66.3	24.3	292	112	501	104	921	177	3058	10.2	12,571	8.12	1130	3241	2.03	3265	−0.1	−0.8	0.7
	0.02	12.0	0.24	2.88	7.67	0.42	36.8	12.6	140	51.7	226	46.5	422	83.6	1446	8.00	11,586	4.47	389	1092	3.81	1100	−0.6		
	0.18	28.0	0.93	13.7	27.0	3.96	120	37.4	398	136	546	104	872	164	3667	7.05	9532	3.52	1057	1139	10.7	1147	−0.1		
	0.08	6.05	0.19	2.82	5.28	0.38	33.0	12.1	155	60.5	280	60.4	548	108	1694	8.77	12,777	10.1	351	1820	3.58	1833	−2.2		
	0.11	15.6	0.76	11.7	18.8	2.74	83.9	25.6	274	94.1	383	74.8	637	123	2568	3.03	8720	1.27	547	628	6.24	633	−0.1		
	0.19	9.59	0.12	1.24	3.32	0.11	22.3	9.64	129	54.2	265	61.0	590	120	1612	18.3	13,429	17.5	790	4149	0.98	4179	−1.0		
	0.01	11.5	0.07	1.25	3.23	0.24	18.6	7.47	98.8	40.1	190	44.9	427	87.4	1183	7.56	12,398	7.15	334	1557	2.09	1568	−0.5		
	0.00	8.18	0.09	1.76	5.41	0.35	34.9	13.8	172	66.7	301	63.4	572	112	1905	16.4	12,603	7.18	519	1988	1.64	2002	−1.1		
	0.07	12.9	0.14	2.06	4.61	0.20	29.4	11.8	154	62.5	295	65.4	618	126	1784	11.5	12,429	9.34	730	2600	2.05	2618	−0.7		
	0.05	5.26	0.05	0.70	1.63	0.06	11.6	4.46	55.9	21.7	97.6	20.9	193	38.7	616	3.62	11,578	1.85	147	373	5.10	376	−1.4		

Magmatic oxygen fugacity is calculated using the method proposed by Loucks (2020).

Table 5
Zircon Hf isotopic data of the Cilincuo, Rongyicuo and Hagela plutons.

Pluton	Age (Ma)	$^{176}Lu/^{177}Hf$	2 σ Err.	$^{176}Hf/^{177}Hf$	2 σ Err.	$(^{176}Hf/^{177}Hf)_i$	$(^{176}Hf/^{177}Hf)_{CHUR}$	εHf (0)	εHf (t)	2 σ Err.	$f_{(Lu/Hf)}$	T_{DM}(Ma)	$T_{DM,2}$(Ma)
Hagela	97.1	0.001348	0.000104	0.282529	0.000018	0.282526	0.282711	−8.6	−6.5	0.6	−1.0	1034	1573
	97.1	0.000651	0.000003	0.282547	0.000019	0.282546	0.282712	−8.0	−5.9	0.7	−1.0	989	1530
	97.1	0.001583	0.000072	0.282495	0.000019	0.282492	0.282712	−9.8	−7.8	0.7	−1.0	1088	1650
	97.1	0.001365	0.000024	0.282504	0.000018	0.282501	0.282712	−9.5	−7.4	0.6	−1.0	1070	1630
	97.1	0.000733	0.000014	0.282558	0.000012	0.282557	0.282712	−7.6	−5.5	0.4	−1.0	976	1505
	97.1	0.001005	0.000011	0.282543	0.000015	0.282541	0.282712	−8.1	−6.0	0.5	−1.0	1004	1541
	97.1	0.000870	0.000050	0.282580	0.000017	0.282578	0.282712	−6.8	−4.7	0.6	−1.0	949	1457
	97.1	0.000609	0.000010	0.282600	0.000015	0.282599	0.282712	−6.1	−4.0	0.5	−1.0	914	1410
	97.1	0.000681	0.000011	0.282535	0.000016	0.282534	0.282712	−8.4	−6.3	0.6	−1.0	1006	1557
	97.1	0.000677	0.000016	0.282548	0.000017	0.282546	0.282712	−7.9	−5.8	0.6	−1.0	989	1529
	97.1	0.000561	0.000013	0.282567	0.000014	0.282566	0.282712	−7.3	−5.2	0.5	−1.0	959	1485
	97.1	0.000649	0.000020	0.282555	0.000016	0.282554	0.282712	−7.7	−5.6	0.5	−1.0	978	1512
	97.1	0.000587	0.000004	0.282623	0.000016	0.282622	0.282712	−5.3	−3.2	0.6	−1.0	882	1360
	97.1	0.000902	0.000006	0.282588	0.000016	0.282586	0.282712	−6.5	−4.4	0.6	−1.0	939	1440
	97.1	0.000906	0.000013	0.282558	0.000017	0.282557	0.282712	−7.6	−5.5	0.6	−1.0	980	1506
	97.1	0.000616	0.000005	0.282561	0.000016	0.282560	0.282712	−7.5	−5.4	0.6	−1.0	969	1499
	97.1	0.000887	0.000004	0.282532	0.000015	0.282530	0.282712	−8.5	−6.4	0.5	−1.0	1017	1565
	97.1	0.001831	0.000023	0.282536	0.000018	0.282533	0.282712	−8.3	−6.3	0.6	−0.9	1037	1559
	97.1	0.000681	0.000027	0.282601	0.000017	0.282600	0.282712	−6.0	−4.0	0.6	−1.0	915	1409
	97.1	0.000983	0.000016	0.282552	0.000018	0.282550	0.282712	−7.8	−5.7	0.6	−1.0	991	1520
	97.1	0.001022	0.000017	0.282541	0.000017	0.282539	0.282712	−8.2	−6.1	0.6	−1.0	1008	1546
	97.1	0.001998	0.000046	0.282512	0.000019	0.282508	0.282712	−9.2	−7.2	0.7	−0.9	1076	1614
	97.1	0.000831	0.000024	0.282626	0.000018	0.282625	0.282712	−5.2	−3.1	0.6	−1.0	883	1353
	97.1	0.000892	0.000005	0.282568	0.000014	0.282566	0.282712	−7.2	−5.1	0.5	−1.0	966	1484
	97.1	0.000929	0.000011	0.282533	0.000016	0.282531	0.282712	−8.5	−6.4	0.6	−1.0	1017	1563
	97.1	0.000661	0.000003	0.282562	0.000015	0.282561	0.282712	−7.4	−5.3	0.5	−1.0	968	1496
	97.1	0.000671	0.000016	0.282588	0.000018	0.282587	0.282712	−6.5	−4.4	0.6	−1.0	933	1438
	97.1	0.000949	0.000008	0.282533	0.000015	0.282531	0.282712	−8.5	−6.4	0.5	−1.0	1017	1564
	97.1	0.001132	0.000038	0.282534	0.000014	0.282532	0.282712	−8.4	−6.4	0.5	−1.0	1020	1561
Cilincuo	86.1	0.001782	0.000062	0.282677	0.000010	0.282674	0.282719	−3.4	−1.6	0.4	−0.9	832	1249
	86.1	0.000921	0.000011	0.282642	0.000011	0.282641	0.282719	−4.6	−2.8	0.4	−1.0	863	1325
	86.1	0.000676	0.000003	0.282637	0.000011	0.282636	0.282719	−4.8	−2.9	0.4	−1.0	865	1336
	86.1	0.000843	0.000006	0.282636	0.000010	0.282634	0.282719	−4.8	−3.0	0.3	−1.0	870	1339
	86.1	0.000915	0.000003	0.282652	0.000009	0.282651	0.282719	−4.2	−2.4	0.3	−1.0	848	1302
	86.1	0.000830	0.000003	0.282623	0.000010	0.282621	0.282719	−5.3	−3.4	0.3	−1.0	888	1368
	86.1	0.001042	0.000014	0.282634	0.000011	0.282633	0.282719	−4.9	−3.0	0.4	−1.0	877	1343
	86.1	0.001213	0.000015	0.282622	0.000008	0.282620	0.282719	−5.3	−3.5	0.3	−1.0	899	1372
	86.1	0.001279	0.000007	0.282654	0.000010	0.282652	0.282719	−4.2	−2.4	0.3	−1.0	855	1300
	86.1	0.000835	0.000007	0.282647	0.000008	0.282646	0.282719	−4.4	−2.6	0.3	−1.0	853	1312
	86.1	0.000719	0.000006	0.282639	0.000009	0.282638	0.282719	−4.7	−2.9	0.3	−1.0	863	1331
	86.1	0.000899	0.000006	0.282657	0.000012	0.282656	0.282719	−4.1	−2.2	0.4	−1.0	841	1291
	86.1	0.000650	0.000007	0.282635	0.000011	0.282634	0.282719	−4.9	−3.0	0.4	−1.0	867	1340
	86.1	0.001136	0.000025	0.282636	0.000011	0.282634	0.282719	−4.8	−3.0	0.4	−1.0	877	1340
	86.1	0.000824	0.000004	0.282650	0.000010	0.282649	0.282719	−4.3	−2.5	0.4	−1.0	849	1306
	86.1	0.000992	0.000013	0.282658	0.000011	0.282657	0.282719	−4.0	−2.2	0.4	−1.0	841	1288
	86.1	0.000802	0.000007	0.282632	0.000010	0.282630	0.282719	−5.0	−3.1	0.4	−1.0	875	1348
	86.1	0.000764	0.000025	0.282630	0.000011	0.282628	0.282719	−5.0	−3.2	0.4	−1.0	877	1352
	86.1	0.000865	0.000004	0.282619	0.000009	0.282618	0.282719	−5.4	−3.6	0.3	−1.0	893	1375
	86.1	0.000833	0.000005	0.282639	0.000009	0.282638	0.282719	−4.7	−2.8	0.3	−1.0	865	1330
	86.1	0.000708	0.000002	0.282636	0.000009	0.282634	0.282719	−4.8	−3.0	0.3	−1.0	867	1338
	86.1	0.001570	0.000079	0.282637	0.000009	0.282634	0.282719	−4.8	−3.0	0.3	−1.0	886	1339
	86.1	0.000868	0.000003	0.282645	0.000008	0.282644	0.282719	−4.5	−2.6	0.3	−1.0	857	1317
	86.1	0.000939	0.000023	0.282661	0.000011	0.282659	0.282719	−3.9	−2.1	0.4	−1.0	837	1283
	86.1	0.000969	0.000010	0.282654	0.000010	0.282652	0.282719	−4.2	−2.3	0.3	−1.0	847	1298
	86.1	0.000818	0.000003	0.282654	0.000010	0.282653	0.282719	−4.2	−2.3	0.4	−1.0	843	1297
	86.1	0.001027	0.000018	0.282618	0.000011	0.282617	0.282719	−5.4	−3.6	0.4	−1.0	899	1379
	86.1	0.002238	0.000022	0.282637	0.000011	0.282634	0.282719	−4.8	−3.0	0.4	−0.9	901	1340
	86.1	0.000966	0.000010	0.282654	0.000011	0.282652	0.282719	−4.2	−2.4	0.4	−1.0	847	1299
Rongyicuo	98	0.001156	0.000058	0.282641	0.000009	0.282639	0.282711	−4.6	−2.6	0.3	−1.0	870	1321
	98	0.001429	0.000019	0.282608	0.000009	0.282606	0.282711	−5.8	−3.7	0.3	−1.0	923	1396
	98	0.001428	0.000049	0.282635	0.000011	0.282632	0.282711	−4.9	−2.8	0.4	−1.0	885	1336
	98	0.001120	0.000032	0.282631	0.000009	0.282629	0.282711	−5.0	−2.9	0.3	−1.0	883	1344
	98	0.000674	0.000022	0.282608	0.000010	0.282607	0.282711	−5.8	−3.7	0.4	−1.0	904	1392
	98	0.001269	0.000005	0.282613	0.000008	0.282610	0.282711	−5.6	−3.6	0.3	−1.0	913	1385
	98	0.001986	0.000037	0.282551	0.000010	0.282547	0.282711	−7.8	−5.8	0.3	−0.9	1020	1526
	98	0.001030	0.000041	0.282606	0.000009	0.282604	0.282711	−5.9	−3.8	0.3	−1.0	917	1400
	98	0.001207	0.000012	0.282592	0.000009	0.282590	0.282711	−6.4	−4.3	0.3	−1.0	940	1431
	98	0.001045	0.000020	0.282598	0.000009	0.282596	0.282711	−6.2	−4.1	0.3	−1.0	928	1417
	98	0.001398	0.000019	0.282599	0.000011	0.282597	0.282711	−6.1	−4.0	0.4	−1.0	935	1415
	98	0.001220	0.000011	0.282616	0.000010	0.282614	0.282711	−5.5	−3.4	0.4	−1.0	906	1377
	98	0.001828	0.000088	0.282644	0.000009	0.282640	0.282711	−4.5	−2.5	0.3	−0.9	881	1317
	98	0.001184	0.000005	0.282607	0.000008	0.282604	0.282711	−5.9	−3.8	0.3	−1.0	919	1398
	98	0.001710	0.000037	0.282608	0.000010	0.282605	0.282711	−5.8	−3.8	0.3	−0.9	930	1397

(*continued on next page*)

Table 5 (*continued*)

Pluton	Age (Ma)	$^{176}Lu/^{177}Hf$	2 σ Err.	$^{176}Hf/^{177}Hf$	2 σ Err.	$(^{176}Hf/^{177}Hf)_i$	$(^{176}Hf/^{177}Hf)_{CHUR}$	εHf (0)	εHf (t)	2 σ Err.	$f_{(Lu/Hf)}$	T_{DM}(Ma)	$T_{DM,2}$(Ma)
	98	0.001430	0.000018	0.282613	0.000008	0.282610	0.282711	−5.6	−3.6	0.3	−1.0	917	1386
	98	0.001295	0.000020	0.282613	0.000008	0.282611	0.282711	−5.6	−3.6	0.3	−1.0	913	1384
	98	0.001468	0.000059	0.282617	0.000012	0.282614	0.282711	−5.5	−3.4	0.4	−1.0	912	1377
	98	0.000713	0.000017	0.282637	0.000010	0.282636	0.282711	−4.8	−2.7	0.3	−1.0	865	1328
	98	0.001390	0.000009	0.282609	0.000008	0.282607	0.282711	−5.8	−3.7	0.3	−1.0	921	1393
	98	0.001778	0.000060	0.282634	0.000011	0.282630	0.282711	−4.9	−2.9	0.4	−0.9	895	1340
	98	0.001326	0.000050	0.282614	0.000009	0.282611	0.282711	−5.6	−3.5	0.3	−1.0	913	1383
	98	0.001878	0.000036	0.282587	0.000010	0.282584	0.282711	−6.5	−4.5	0.3	−0.9	965	1445
	98	0.001161	0.000013	0.282610	0.000009	0.282608	0.282711	−5.7	−3.7	0.3	−1.0	914	1391
	98	0.001602	0.000038	0.282602	0.000010	0.282599	0.282711	−6.0	−4.0	0.4	−1.0	937	1411
	98	0.001351	0.000010	0.282616	0.000010	0.282614	0.282711	−5.5	−3.5	0.3	−1.0	910	1378
	98	0.001681	0.000030	0.282576	0.000009	0.282573	0.282711	−6.9	−4.9	0.3	−0.9	975	1468

$\varepsilon_{Hf(t)}$ values are calculated using present-day $(^{176}Lu/^{177}Hf)CHUR = 0.0332$ and $(^{176}Hf/^{177}Hf)_{CHUR} = 0.282772$ (Blichert-Toft and Albarède, 1997). T_{DM2} values are calculated using present-day $(^{176}Lu/^{177}Hf)_{DM} = 0.0384$ and $(^{176}Hf/^{177}Hf)_{DM} = 0.28325$ (Griffin et al., 2000). The decay constant of ^{176}Lu is 1.865×10^{-11} yr^{-1} (Scherer et al., 2001). $^{176}Hf/^{177}Hf$ value for the average continental crust is 0.015 (Griffin et al., 2002).

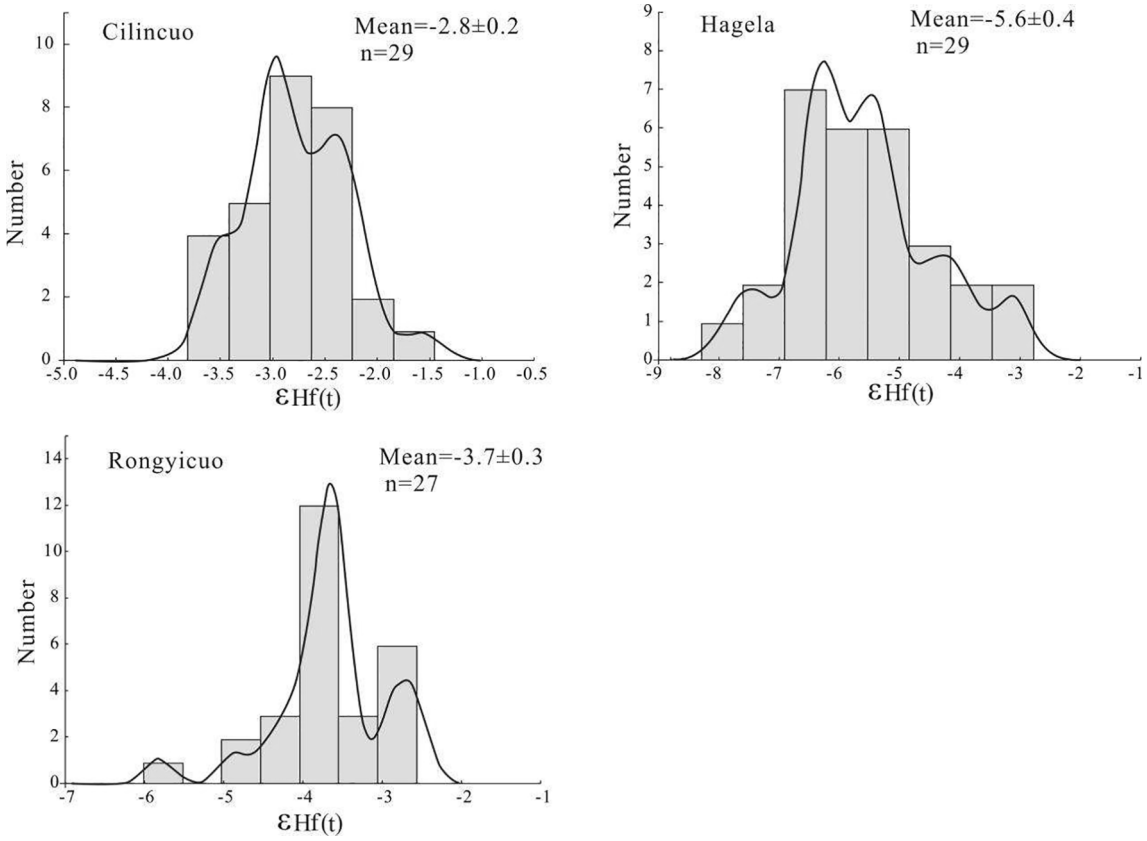

Fig. 6. Histogram of zircon $\varepsilon_{Hf}(t)$ values of the Cilincuo, Rongyicuo, and Hagela plutons.

analyses from the Rongyicuo pluton (98.0 Ma) yielded $\varepsilon_{Hf}(t)$ values between − 5.8 and − 2.5 with T_{DM2} model ages of 1.32–1.53 Ga.

4.4. Whole-rock Sr–Nd isotope compositions

The values of $(^{87}Sr/^{86}Sr)_I$ and $\varepsilon_{Nd}(t)$ were calculated at t = 86.1 Ma for Cilincuo, t = 98.0 Ma for Rongyicuo, and t = 97.1 Ma for Hagela. The Sr–Nd isotopic data are listed in Table 6. The $(^{87}Sr/^{86}Sr)_i$ values (0.7075–0.7076) were lower in the Cilincuo pluton than in the Rongyicuo (0.7095–0.7109) and Hagela (0.7110–0.7114) plutons. The Cilincuo pluton exhibited higher $\varepsilon_{Nd}(t)$ values from − 5.2 to − 4.8, and the Rongyicuo and Hagela plutons showed lower $\varepsilon_{Nd}(t)$ values from − 5.3 to − 6.6 and − 5.5 to − 5.9, respectively. The two-stage Nd model ages (T_{DM2}) were 1.27–1.31 Ga in the Cilincuo pluton, 1.33–1.43 Ga in the Rongyicuo pluton, and 1.34–1.38 Ga in the Hagela pluton.

4.5. Major compositions of apatite

The apatite major elemental composition is listed in Table 7. All analyzed apatite crystals were F-rich (F: 2.54–3.26 wt%). The apatite from the Cilincuo pluton contained more Cl (Cl: 0.04–0.09 wt%) than that from the Rongyicuo and Hagela plutons (< 0.04 wt%). We calculated the mole fractions of fluorapatite, chlorapatite, and hydroxyapatite based on the method proposed by Piccoli and Candela (2002). The results showed that the Cilincuo pluton had a higher mole fraction of hydroxyapatite and chlorapatite (chlorapatite: 0.5–1%; hydroxyapatite:

Table 6
Sr–Nd isotopic data of the Cilincuo, Rongyicuo and Hagela plutons.

Plutons	Sample no.	Age(Ma)	$^{87}Rb/^{86}Sr$	$^{87}Sr/^{86}Sr$	2 σ Err.	$(^{87}Sr/^{86}Sr)_i$	$^{147}Sm/^{144}Nd$	$^{143}Nd/^{144}Nd$	2 σ Err.	$(^{143}Nd/^{144}Nd)i$	εNd (t)	TDM(Ma)	TDM2(Ma)
Cilincuo	CLC-1	86.1	1.54	0.709349	0.000008	0.707463	0.100297	0.512339	0.000006	0.512283	−4.8	1089	1274
	CLC-2	86.1	1.70	0.709632	0.000010	0.707558	0.109585	0.512345	0.000008	0.512283	−4.8	1178	1274
	CLC-3	86.1	1.49	0.709421	0.000009	0.707603	0.105616	0.512340	0.000008	0.512280	−4.8	1142	1278
	CLC-4	86.1	1.53	0.709516	0.000009	0.707641	0.104920	0.512319	0.000006	0.512260	−5.2	1164	1311
Hagela	HGL-2	97.1	3.10	0.715657	0.000011	0.711377	0.120458	0.512286	0.000008	0.512209	−5.9	1411	1377
	HGL-3	97.1	3.00	0.715520	0.000011	0.711381	0.125648	0.512294	0.000006	0.512214	−5.8	1480	1370
	HGL-5	97.1	3.09	0.715287	0.000013	0.711028	0.127267	0.512313	0.000010	0.512233	−5.5	1473	1340
Rongyicuo	RYC-3	98	3.27	0.715305	0.000012	0.710748	0.116498	0.512257	0.000007	0.512182	−6.4	1399	1419
	RYC-4	98	3.16	0.715266	0.000012	0.710867	0.111252	0.512246	0.000006	0.512175	−6.6	1343	1431
	RYC-5	98	2.85	0.713502	0.000010	0.709527	0.110317	0.512310	0.000008	0.512239	−5.3	1237	1328

$\varepsilon_{Nd(t)}$ values are calculated using present-day $(^{147}Sm/^{144}Nd)_{CHUR} = 0.1967$ and $(^{143}Nd/^{144}Nd)_{CHUR} = 0.512638$. T_{DM} values are calculated using present-day $(^{147}Sm/^{144}Nd)_{DM} = 0.2137$ and $(^{143}Nd/^{144}Nd)_{DM} = 0.51315$. The details for two-stage (T_{DM2}) Nd model age calculations are given by Wu et al. (2002). Two-stage Nd model age (T_{DM2}) is calculated using the same formulation as Keto and Jacobsen (1987).

19–30%) than the Rongyicuo (chlorapatite: 0.2–0.4%; hydroxyapatite: 14–22%) and Hagela plutons (chlorapatite: 0.1–0.5%; hydroxyapatite: 10–20%).

5. Discussion

5.1. Ages and tectonic environment of granite formation

Although the closure time of the Garzê-Litang Ocean remains controversial (Huang et al., 2018; Yan et al., 2019; Wang et al., 2021), it is generally recognized that after the disappearance of the Garzê-Litang Ocean in the Late Triassic, this region has not experienced the opening and extinction of oceans (Hou et al., 2007; Li et al., 2017). Moreover, in the discriminant diagram of granite related tectonic background (Pearce 1996), all of rock samples fall within the field of the within plate granite (Fig. 3**c, d**). Combining petrogeochemical characteristics with zircon U-Pb ages ranging from 98 to 85 Ma, it can be concluded that the formation of investigated granite plutons occurred in the intra-continental extensional setting without ocean slab subduction.. However, the geodynamic setting that triggered regional intra-continental extension in the Late Cretaceous is still debatable.

A popular view has ascribed the Late Cretaceous intra-continental extension to lithospheric delamination after the collision between the Songpan-Garzê block and Yidun Terrane (Hou et al., 2001, 2003; Qu et al., 2002). An alternative model has proposed in recent years (e.g., Wang et al. 2014c, 2019), in which reported a NS–NNW-directed Late Cretaceous transtension in the Eastern Tibetan Plateau following the Lhasa-Qiangtang collision. This extension is interpreted to have been triggered by Bangong-Nujiang slab break-off driven by the far-field subduction of the Neo-Tethys oceanic crust at ~ 110 Ma, and ultimately induced Cretaceous magmatism in this region. A key to this dispute is the time interval between the *syn*-collision and post-collisional magmatism. The first model suggests a relatively long time interval (>100 Ma). However, in consideration of some intra-continental felsic volcanics and A-type granites with ages of 190–180 Ma in the Songpan–Garzê block (e.g., Hu et al., 2005; Zhao et al., 2007), the post-collisional magmatism in response to the collision between the Songpan-Garzê block and Yidun Terrane can be more likely to have occurred in the Early Jurassic rather than the Late Cretaceous. Therefore, we are more in favor of the second model, although the possibility of the first model cannot be entirely ruled out.

5.2. Geochemical affinities of the three plutons

Previous studies have considered the Late Cretaceous granites in this region as A-type, S-type, or I-type granites (Hou et al., 2007; Wu et al., 2014; Yang et al., 2016). Typical S-type granites are strongly peraluminous (A/CNK > 1.1) because they are derived from melting of Al-rich metapelite (Chappell and White, 2001). In contrast, the Cilincuo and Rongyicuo plutons are metaluminous to weakly peraluminous (A/CNK: 0.94–1.05 in Cilincuo; 0.99–1.05 in Rongyicuo; and 1.03–1.11 in Hagela). Moreover, the decrease in P_2O_5 content with increasing SiO_2 content (Fig. 7**a**) and K/Rb ratio (Fig. 8**a**) in the three investigated plutons contradicts the consensus that the P content increases with increasing fractionation in S-type melts because apatite is soluble in peraluminous melts (Chappell, 1999). Finally, the variation in whole-rock Rb and Y contents of these three plutons are deviated from the accepted evolution trend of those two elements in S-type melts (Zhu et al., 2018a, Fig. 8**b**).

Our data show that all samples of the Cilincuo and Hagela plutons and two samples of the Rongyicuo pluton have high 10000 Ga/Al and FeO_T/MgO ratios and Zr + Nb + Ce + Y values, all of which fall within the field of A-type granite (Whalen et al., 1987; Fig. 9**a, b**). However, three samples of the Rongyicuo pluton can not fall within this field because of the relatively low Zr + Nb + Ce + Y values that may result from the fractional crystallization of zircon and allanite during magma

Table 7
the major elements concentration (wt.%) of apatite from the Cilincuo, Rongyicuo and Hagela plutons.

Plutons	Hagela									
Spot no.	1	2	3	4	5	6	7	8	9	10
MnO	0.13	0.16	0.13	0.13	0.20	0.18	0.16	0.12	0.18	0.13
CaO	54.58	54.74	54.54	54.49	52.53	54.33	54.80	53.61	54.73	53.43
Na_2O	0.11	0.15	0.23	0.15	0.14	0.20	0.22	0.15	0.13	0.20
P_2O_5	40.75	41.32	41.00	40.81	38.63	40.96	41.12	39.58	40.93	39.64
F	3.26	3.13	3.07	3.10	3.19	3.12	3.08	3.20	2.96	3.00
FeO	0.08	0.09	0.07	0.04	0.07	0.08	0.07	0.10	0.08	0.10
Cl	0.02	0.02	0.02	0.03	0.03	0.02	0.04	0.02	0.02	0.01
Total	98.92	98.29	97.76	97.44	94.27	97.59	98.19	95.82	97.79	95.64
FAP	88.0%	84.2%	83.0%	83.9%	89.4%	84.7%	82.7%	88.1%	79.8%	82.7%
CAP	0.2%	0.3%	0.3%	0.5%	0.4%	0.3%	0.5%	0.2%	0.3%	0.2%
HAP	11.7%	15.4%	16.7%	15.6%	10.2%	15.0%	16.7%	11.7%	19.9%	17.1%
Cl in magma (ppm)	200	288	275	388	313	250	438	188	225	125

FAP, CAP and HAP are the mole fraction of fluorapatite, chloraptite and hydroxylaptite, which are calculated based on the method of Piccoli and Candela (2002); Partition coefficients of F and Cl are from Parat et al.(2011). Dcl apatite/melt = 0.8.

evolution. Furthermore, a large number of statistical data have shown that with a decrease in Zr content, the 10000 Ga/Al ratio will increase in I-type granite, while will decrease in A-type granite (Wu et al., 2017a). The observed positive correlation between the whole-rock Ga/Al ratio and Zr content agrees the change of these indexes in A-type granite (Fig. 9**c**). In addition, the ratios of Sr/Y, La/Yb, and Eu/Eu* of the three plutons are completely different from those of the I-type granites in the Yidun Terrane, such as Tongchanggou and Relin (e.g., Wang et al., 2014b). Based on the above findings, we suggest that the three plutons can be classified as A-type granite.

5.3. Magma compositions and evolution

In this study, all rock samples from the three plutons show high SiO_2 values and low CaO (0.39–1.67 wt%), MgO (0.01–0.57 wt%), and Sr (10.1–256 ppm) values. These geochemical characteristics indicate that the causative magmas have undergone extensive differentiation. The range of whole-rock Zr/Hf and Nb/Ta values (Wu et al., 2017a; Fig. 9**d**) supports the classification of the studied plutons as highly fractionated granites. The clear decreasing trends in the contents of Fe_2O_{3T}, CaO, MgO, and TiO_2 with increasing SiO_2 content (Fig. 7**b–e**) correspond well to the fractional crystallization of biotite and amphibole. The simultaneous reduction of whole-rock SiO_2, Al_2O_3, and Eu/Eu* values in the Hagela and Rongyicuo plutons (Fig. 7**f, g**) can be caused by significant feldspar fractionation (e.g., Ballard et al., 2002; Bi et al., 2002). These positive correlations, however, are not obvious in the Cilincuo pluton (Fig. 7**f, g**). Coupled with the limited range of whole-rock Sr, Ba, and Eu/*Eu values (Fig. 10**a, b**), we deduced that only a small number of feldspars can be fractionated during magma evolution of this pluton.

The suppression of fractional crystallization of feldspar, which will increase Sr and Eu in the whole rock, could result from the high water content in the magma. The abundant water, in turn, induces the early fractionation of amphibole and causes a depletion of Y and Yb in the whole rock (Richards, 2011; Loucks, 2014). For this reason, the higher Sr/Y and Eu/Eu* values in the Cilincuo pluton compared to those in the Rongyicuo and Hagela plutons may be indicative of a more hydrous magma system of the former pluton. Likewise, the Cilincuo pluton apatite has a higher mole fraction of hydroxyapatite than that from the Hagela and Rongyicuo plutons (Fig. 11). Moreover, the calculated magmatic Cl abundances using the apatite/melt partition coefficients reported by Parat et al. (2011) show that the parental magma of the Cilincuo pluton is richer in Cl (488–1113 ppm) than those of the Hagela (Cl: 125–438 ppm) and Rongyicuo (Cl: 75–338 ppm) plutons (Table 7).

Porphyry Cu ± Mo mineralization is usually considered to be linked with adakite (Richards and Kerrich, 2007; Richards, 2011). This type of igneous rock may have been formed by a hydrous magma system (even H_2O > 10 wt%; Lu et al., 2015) and characterized by high whole- rock Sr/Y (>40) and Eu/Eu* (close to one) values (Defant and Drummond, 1990). However, the whole-rock Sr/Y and Eu/Eu* values in the plutons investigated were all lower than those in typical adakite. Moreover, the three plutons contain less hydroxyapatite (mole fraction: 10–31%) and chlorapatite (mole fraction 0.1–1.3%) than other Cu-mineralized plutons in this region, such as Pulang (hydroxyapatite mole fraction 26–36% and chlorapatite of 0.5–7.9% calculated using the data from Pan et al., 2020) (Fig. 11). The calculated magmatic Cl content of the three plutons studied (Table.7) was also lower than that in the Cu-mineralized magmas in other studies (e.g., Zhu et al., 2018b). In addition, we compared the above three plutons with the coeval Mo and Cu mineralized Tongchanggou pluton located in the sourthern Yidun Terrane. Whole-rock chemical composition from Pan et al. (2016) shows that the Tongchanggou pluton is adakite and has high Sr/Y (55–65) and Eu/Eu* (0.96–1.01) values. The calculated mole fractions of hydroxyapatite (31–48%) and chlorapatite (1–2%) in the the Tongchanggou pluton using the chemical composition of apatite from Gao et al. (2020) are also higher than those in the three selected plutons. These findings further suggest that the magma systems of the plutons investigated do not have the enrichment in H_2O and Cl required for porphyry Cu ± Mo mineralization.

In the Harker diagrams, whole-rock P_2O_5 and Zr values correlate negatively with SiO_2 (Fig. 7**a, h**), indicating the fractional crystallization of apatite and zircon, respectively, during magma evolution. This process further results in the observed trend of decreasing REE with increasing SiO_2 content in the Cilincuo and Rongyicuo plutons because of the high REE partition coefficient of the accessory minerals that were removed from the evolving magma (Henerson, 1980; Nardi et al., 2013) (Fig. 7**i**). REEs are a group of elements with similar geochemical behavior and can fractionate from each other due to the fractional crystallization of accessory minerals (e.g., Evans and Hanson, 1993; Dahlquist, 2001). In this study, the La/Yb ratio was observed to decrease dramatically with the increase in SiO_2 content in the Rongyicuo pluton (Fig. 7**j**) and to increase slightly in the Hagela pluton. These completely opposite evolution trends may be related to the fractionation of different accessory mineral assemblages in the two magma systems. Continuous fractional crystallization of zircon, which is much more compatible with Yb than La (Nardi et al., 2013), could have caused the simultaneous increase in the whole- rock La/Yb ratio and SiO_2 content in the Hagela pluton. In contrast, the decreasing La/Yb ratio with increasing SiO_2 content may have resulted from constant fractional crystallization of allanite that can be observed in the Rongyicuo pluton given the high enrichment of La of allanite (Giere and Sorensen, 2004).

5.4. Magma oxidation states

The whole-rock Fe^{3+}/Fe^{2+} ratio is a popular index for the magma

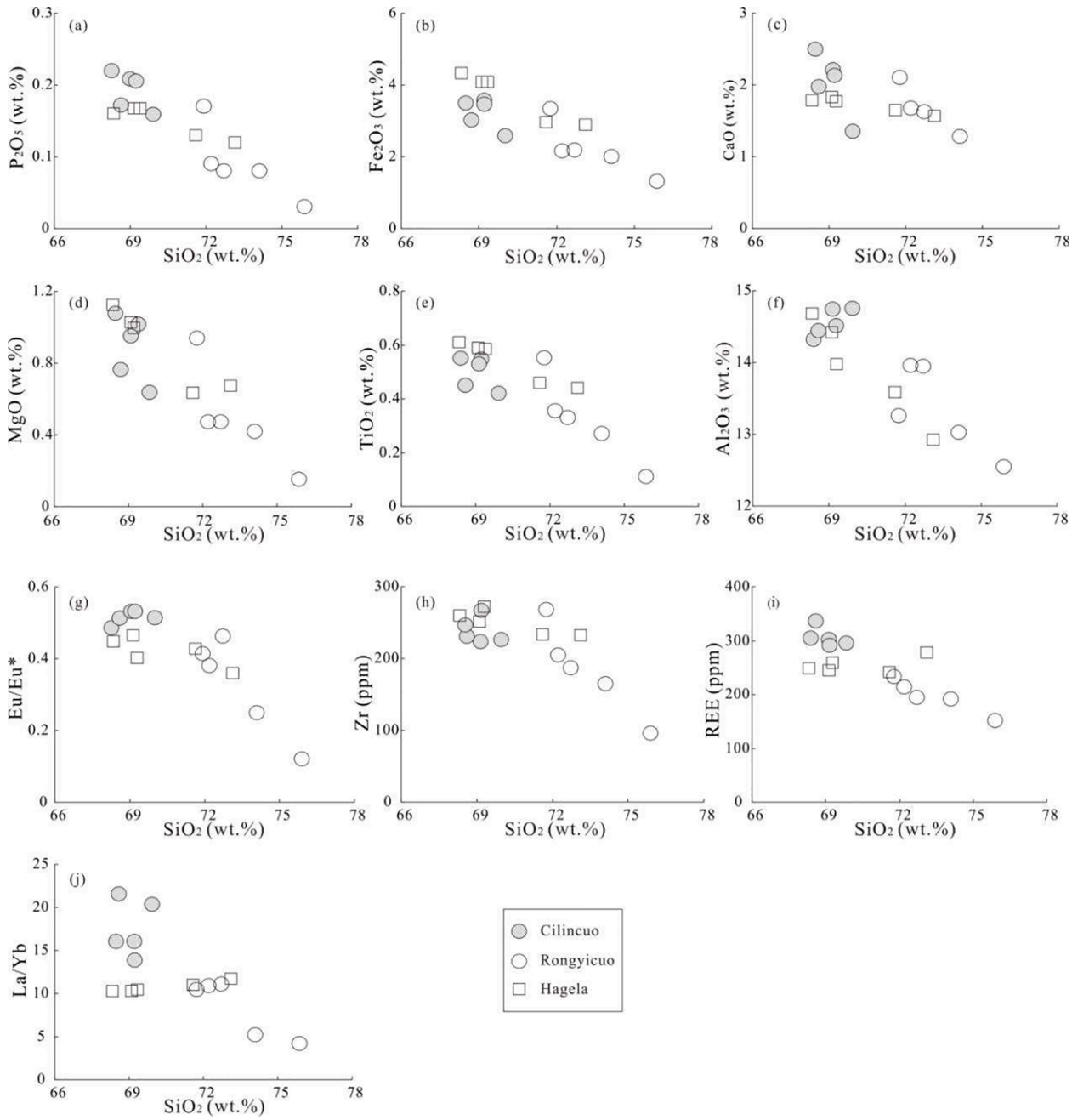

Fig. 7. Elemental contents and ratios variations for the Cilincuo, Rongyicuo, and Hagela plutons.

oxidation state (e.g., Richards, 1990). Our results show that the Cilincuo pluton has a higher Fe^{3+}/Fe^{2+} ratio than the Hagela and Rongyicuo plutons. This finding indicates a higher fO_2 condition in the former pluton than in the latter two plutons. However, the whole-rock Fe^{3+}/Fe^{2+} ratio is easily affected by weathering and alteration, and other evidence is needed to reach this conclusion.

Recently, a new method for estimating the magma oxidation state as zircon crystallized was proposed by Loucks et al. (2020), using ratios of Ce, U, and Ti in zircon, without explicit ionic charge determination, and without independent determination of crystallization temperature, pressure, or parental melt composition. The calculated result using this method (Fig. 12) shows that the Cilincuo pluton parental magma is indeed more oxidized (△FQM −0.3) than other two plutons (△FQM −1.2 and △FQM −0.8, respectively), which is consistent with whole-rock Fe^{3+}/Fe^{2+} ratios.

Many studies have shown that high fO_2 of magma (> △FQM + 1.5) is necessary for porphyry Cu ± Mo mineralization (Mungall, 2002; Sun et al., 2013; 2015; Zhang et al., 2017). Under these redox conditions, S ions are mainly present in the form of S^{6+} (Jugo et al., 2005), which can effectively prevent the exhaustion of ore-forming elements in the melt due to early sulfide crystallization. It is evident that the estimated fugacity values of the three plutons are lower than the recognized fugacity values required for porphyry Cu ± Mo mineralization. Furthermore, using the method proposed by Loucks et al (2020), we calculated magmatic oxygen fugacity of the Mo and Cu mineralized Tongchanggou pluton based on available zircon data from He et al. (2019). The result shows that the parental magma of the Tongchanggou pluton is indeed more oxidized (△FQM + 1.3) than those of the Cilincuo, Hagela and Rongyicuo plutons. In addition, the whole-rock Fe^{3+}/Fe^{2+} ratio of above three plutons (< 0.26) are all lower than that of other Cu and Mo mineralized plutons in this region such as Pulang and Tongchanggou (whole-rock Fe^{3+}/Fe^{2+} ratio: 0.29–0.69; Pan et al.,

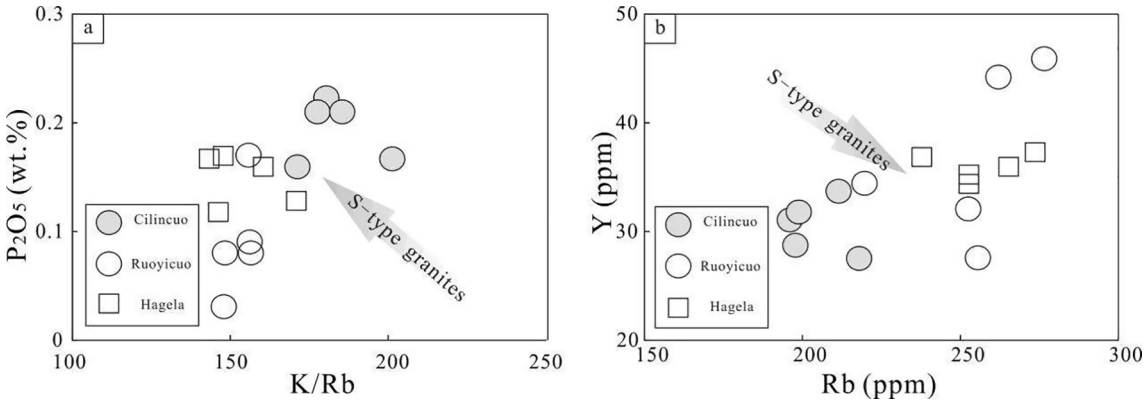

Fig. 8. Plots of K/Rb vs. P_2O_5 (a) and Rb vs. Y (b).

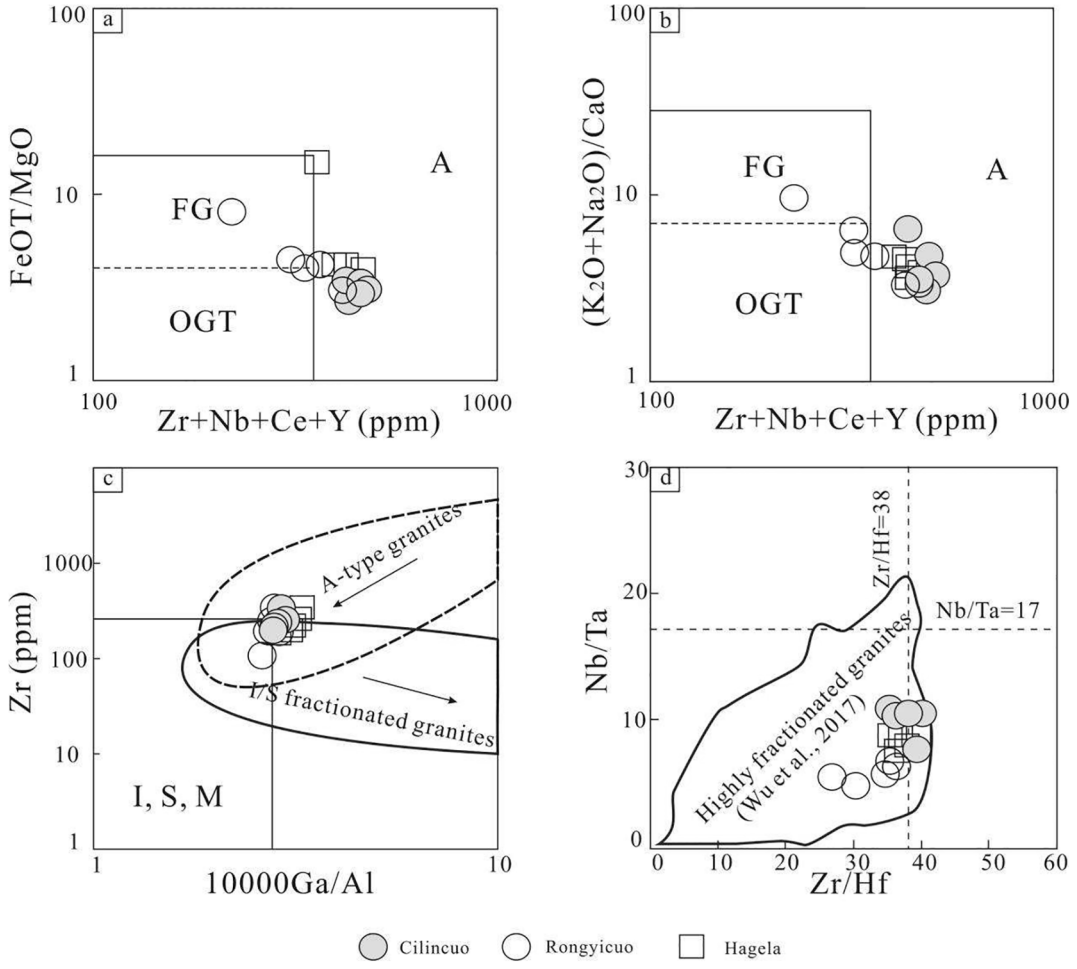

Fig. 9. Discriminant diagram of granite types in the northern Yidun Terrane FeO_T/MgO vs. Zr + Nb + Ce + Y diagram (Whalen et al., 1987) (a); $(K_2O + Na_2O)/CaO$ vs. Zr + Nb + Ce + Y diagram (Whalen et al., 1987) (b) ; Zr vs. 1000 Ga/Al diagram (Whalen et al., 1987) (c); (4) Nb/Ta vs. Zr/Hf diagram (According to Wu et al., 2017a). FG = fractionated M-, I-, and S-type granites; OGT = unfractionated M-, I-, and S-type granites (d).

2016) (Fig. 12). Together with the deficiency of H_2O and Cl in magma, a high potential of these plutons is not expected to form important porphyry Cu and Mo deposits.

5.5. Infertile magma source

Our data show that the Cilincuo pluton contains higher whole-rock $\varepsilon_{Nd}(t)$ and zircon $\varepsilon_{Hf}(t)$ values and lower whole-rock $(^{87}Sr/^{86}S)_i$ values than the other two plutons. These isotopic signatures imply that the former pluton was likely formed by a magma system composed of more mantle components. A previous study, based on a positive correlation between the Cu reserves of porphyry deposits and the $\varepsilon_{Hf}(t)$ value of host rocks in the Gangdese metallogenic belt (Hou et al., 2013b), proposed that the addition of mantle material can be favorable for porphyry Cu mineralization, perhaps because Cu in magma that formed in the intracontinental setting mainly comes from lithospheric mantle (Hou et al., 2020). Therefore, it can be inferred that the increase in mantle-derived materials in magma is partly responsible for the elevated Cu

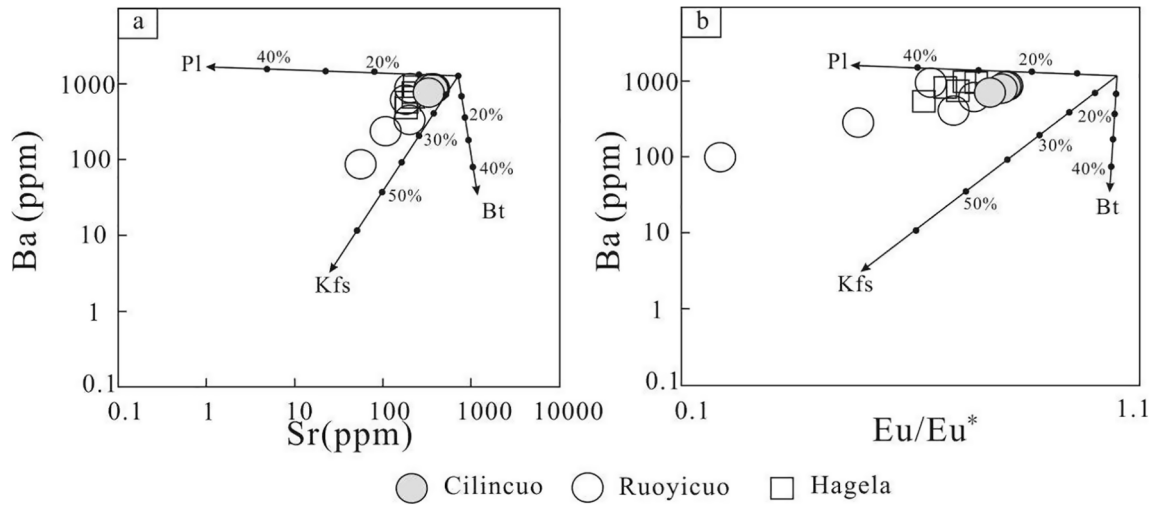

Fig. 10. Ba vs. Sr (a) and Ba vs. Eu/Eu* (b) plots for the selected three plutons. Vectors for plagioclase (Pl), K-feldspar (Kfs), and biotite (Bt) fractionation are cited from Wang et al. (2014c).

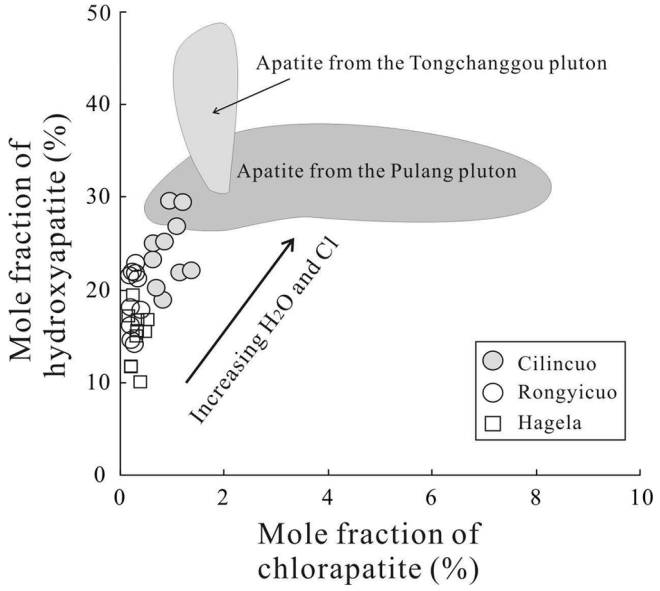

Fig. 11. Mole fraction of chlorapatite vs. hydroxyapatite in the selected three plutons. The apatite data of the Pulang pluton are from Pan et al.(2020) and those from the Tongchanggou pluton are from Gao et al. (2020).

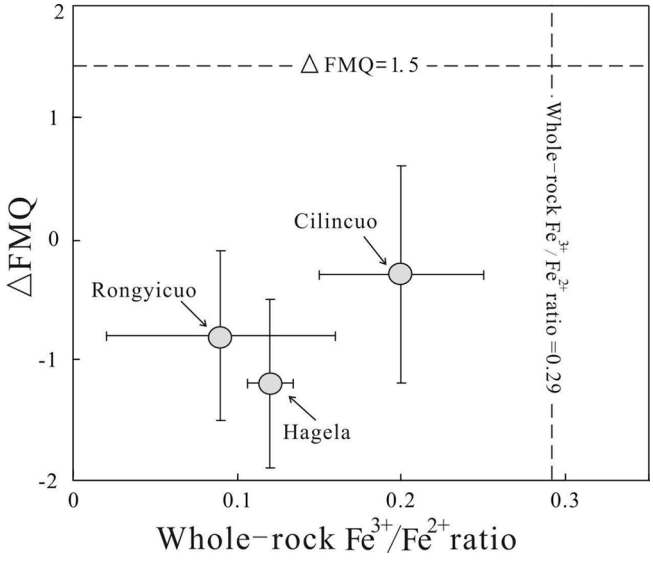

Fig. 12. Magma oxidation states of the selected three plutons.

mineralization ability of the Cilincuo pluton relative to the Hagela and Rongyicuo plutons. Moreover, despite the small amount of whole-rock Sr-Nd isotope data, a negative correlation between $(^{87}Sr/^{86}Sr)_i$ and MgO content (Fig. 13**a**) plus a positive correlation between $(^{143}Nd/^{144}Nd)_i$ and MgO content in the Rongyicuo pluton (Fig. 13**b**) indicate assimilation and contamination during petrogenesis (e.g., Wang et al., 2018b; Li et al., 2019). The diorite enclaves in the Rongycuo pluton, which are interpreted as a result of the contamination of felsic magma by basic material also support this conclusion (Yin 2018). However, $(^{87}Sr/^{86}Sr)_i$ and $(^{143}Nd/^{144}Nd)_i$ do not show a good correlation with the MgO content in the Hagela and Cilincuo plutons, perhaps suggesting negligible assimilation and contamination during magma evolution.

By comparison, the Sr-Nd isotopic compositions of three investigated plutons are clearly different from those of the Late Cretaceous plutons associated with porphyry Cu ± Mo mineralization in the Yidun Terrane, such as the Hongshan, Relin, and Tongchanggou. However, these plutons contain similar Sr-Nd isotope compositions to the Late Triassic granites in this region, such as Sucuoma, Cuojiaoma, and Dongcuo, which are all not capable of porphyry Cu and Mo mineralization (Fig. 13**c**). Previous studies concluded that the magma source of these non -mineralized Late Triassic granite plutons was a mixture of the Proterozoic Kangding Complex, which was derived from the Yangtze Craton and metasedimentary rock from the basement in different proportions (Wu et al., 2017b). A recent study from Wang et al. (2020) further proposed that the absence of oxidized and hydrous Neoproterozoic arc root remnant might cause the infertility of such a magma source. On the contrary, the pluton derived from a magma source containing Neoproterozoic arc root remnant could form porphyry Cu deposit such as Pulang. It can be thus speculated that the re-melting of this infertile source, which was triggered by intra-continental extension during the Late Cretaceous, formed widespread Cu- and Mo- infertile granite plutons in this region.

Finally, we evaluated the possibility of uplift and erosion of the plutons leading to the absence of porphyry Cu-Mo deposits. A previous study has shown that the Cenozoic thermal evolution of the entire Yidun Terrane involved an early stage of relatively rapid erosion and a late

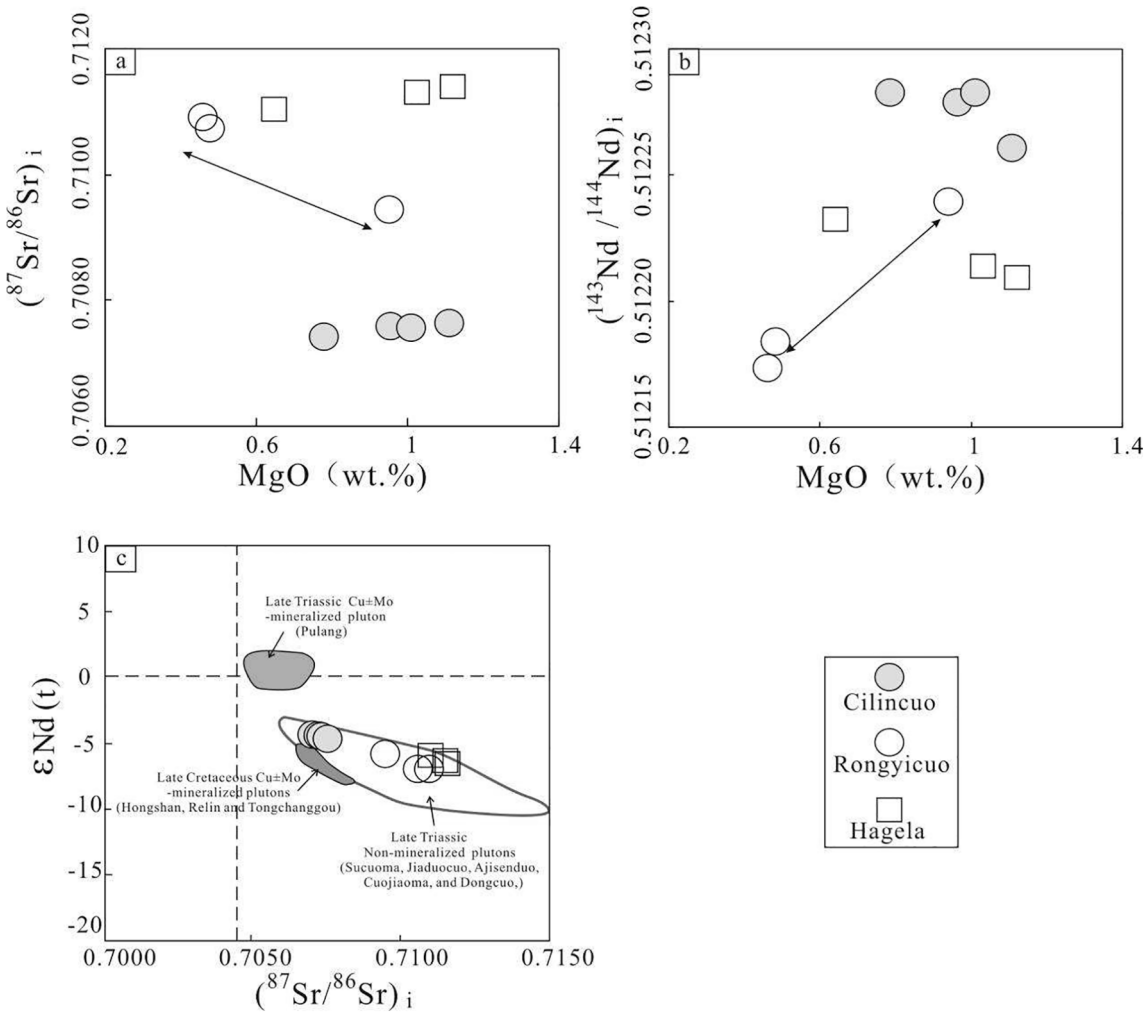

Fig. 13. MgO vs. $(^{87}Sr/^{86}Sr)_i$ (a); MgO vs. $(^{143}Nd/^{144}Nd)_i$ (b); $\varepsilon_{Nd}(t)$ and $(^{87}Sr/^{86}Sr)_i$ diagram of the selected three plutons (c). The trends of the Pulang pluton are from Wang et al. (2018). The trends of the Late Cretaceous Cu ± Mo mineralized plutons are from Wang et al. (2014b) . The trends of the Late Triassic non-mineralization plutons are from Wu et al. (2017b).

stage of much slower erosion (Leng et al., 2018). During this uplift and erosion history, 1000–3000 m thickness of materials have been removed, such as that happened in Pulang and Xiuwacu (Leng et al., 2018; Zhang et al., 2021). Given the shallow emplacement depth (usually less than 5–8 km) of the magma associated with porphyry Cu-Mo mineralization (Candela and Holland, 1986; Candela 1997), the pre-existing deposits might not be well preserved owing to the erosion of the plutons. However, if the erosion is intense enough to entirely remove the pre-existing porphyry Cu-Mo deposits in the interior of plutons, accordingly, the Ag-Pb-Zn deposits of magmatic-hydrothermal origin in the periphery of these plutons should also be eliminated. This scenario is contradictory to the retention of Ag-Pb-Zn deposits such as Xiasai and Shaxi. Therefore, we speculate that the erosion of pluton can not well explain the absence of Cu and Mo deposits. Instead, the inadequacy of magma fertility revealed by this study is a fundamental reason for the failure of granite plutons in the Northern Yidun Terrane to generate Cu and Mo mineralization.

6. Conclusions

The Cilincuo, Rongyicuo, and Hagela plutons formed in Late Cretaceous intracontinental setting (98–86.1 Ma) which can be classified as A-type granite that underwent a high-degree of magma differentiation.

The chemical compositions of apatite, zircon, and their host rocks reveal that the parental magma of the Cilincuo pluton is more oxidized and H_2O-Cl rich than those of the Rongyicuo and Hagela plutons.

The reasons for the Cu–Mo infertility of the three plutons are the low H_2O-Cl content and oxygen fugacity of the causative magmas, which may be related to an infertile magma source.

Declaration of Competing Interest

The authors declare that they have no known competing financial interests or personal relationships that could have appeared to influence the work reported in this paper.

Acknowledgments

This study was supported by the project of “Innovative Team of One Belt and One Road” of the Chinese Academy of Sciences, the Science and Technology Foundation of Guizhou Province (QKHJC-ZK[2021] YB 211), the National Natural Science Foundation of China (Grant 41703050), the Strategic Priority Research Program (B) of the Chinese Academy of Sciences (XDB18000000) and “Light of West China” Program of Chinese Academy of Sciences. We thank Yan-Wen Tang for his assistance in zircon U-Pb dating and trace element analysis by LA-ICP-MS, Wen-Qin Zheng and Xiang Li for their support in apatite major

elements analysis by EPMA, Jing Hu and Shu-Qin Yang for their assistance in the whole-rock chemical analysis by XRF and ICP-MS and Dr. Ting Zhou for his assistance in the whole-rock Sr-Nd isotope analysis by MC-ICP-MS.

References

Ballard, J.R., Palin, M.J., Campbell, I.H., 2002. Relative oxidation states of magmas inferred from $Ce^{(IV)}/Ce^{(III)}$ in zircon: application to porphyry copper deposits of Northern Chile. Contrib. Miner. Petrol. 144 (3), 347–364.

Bi, X.W., Cornell, D.H., Hu, R.Z., 2002. REE composition of primary and altered feldspar from the mineralized alteration zone of alkali-rich intrusive rocks, Western Yunnan Province, China. Ore. Geol. Rev. 19, 69–78.

Blichert-Toft, J., Albarède, F., 1997. The Lu–Hf isotope geochemistry of chondrites and the evolution of the mantle–crust system. Earth Planet. Sci. Lett. 148 (1-2), 243–258.

Candela, P.A., Holland, H.D., 1984. The partitioning of copper and molybdenum between silicate melts and aqueous fluids. Geochim. Cosmochim. Acta 48 (2), 373–380.

Candela, P.A., Holland, H.D., 1986. A mass transfer model for copper and molybdenum in magmatic hydrothermal system: the origin porphyry-type ore deposits. Econ. Geol. 81, 1–19.

Candela, P.A., 1997. A review of shallow, ore-related granite: textures, volatiles, and ore metals. J. Petrol. 38, 1619–1633.

Chappell, B.W., 1999. Aluminium saturation in I- and S-type granites and the characterization of fractionated haplogranites. Lithos 46 (3), 535–551.

Chappell, B.W., White, A.J.R., 2001. Two contrasting granite types: 25 years latter. Aust. J. Earth Sci. 48, 489–499.

Cook, D.R., Hollings, P., Walshe, J., 2005. Giant porphyry deposits: Characteristics, distribution, and tectonic controls. Econ. Geol. 100, 801–818.

Dahlquist, J.A., 2001. REE fractionation by accessory minerals in epidote-bearing metaluminous granitoids from the Sierras Pampeanas, Argentina. Mineral. Mag. 65 (4), 463–475.

Defant, M.J., Drummond, M.S., 1990. Derivation of some modern arc magmas by melting of young subducted lithosphere. Nature 347 (6294), 662–665.

Deng, J., Wang, Q., Li, G., Li, C., Wang, C., 2014. Tethys tectonic evolution and its bearing on the distribution of important mineral deposits in the sanjiang region. SW China. Gondwana Res. 26 (2), 419–437.

Evans, O.C., Hanson, G.N., 1993. Accessory-mineral fractionation of rare-earth element (REE) abundances in granitoid rocks. Chem. Geol. 110 (1-3), 69–93.

Fei, G.C., Li, Y.G., Chen, J., 2015. Zircon U-Pb geochronology and geochemistry of copper-bearing monzogranite in the Rexiang hydrothermal Cu deposit in the central Yidun Island Arc, northeastern Tibet. Geochem. J. 49, 195–205.

Gao, X., Yang, L.-Q., Meng, J.-Y., Zhang, L.-J., 2017. Zircon U-Pb, molybdenite Re–Os geochronology and Sr–Nd–Pb–Hf–O–S isotopic constraints on the genesis of Relin Cu–Mo deposit in Zhongdian, Northwest Yunnan. China. Ore Geol. Rev. 91, 945–962.

Gao, X., Yang, L., Wang, C., He, W., Bao, X., Zhang, S., 2020. Halogens and trace elements of apatite from Late Mesozoic and Cenozoic porphyry Cu-Mo-Au deposits in SE Tibet, China: Constraints on magmatic fertility and granitoid petrogenesis. J. Asian Earth Sci. 203, 104552. https://doi.org/10.1016/j.jseaes.2020.104552.

Giere, R., Sorensen, S.S., 2004. Allanite and other REE-rich epidote-group minerals. Rev. Mineral. Geochem. 56 (1), 431–493.

Griffin, W.L., Pearson, N.J., Belousova, E., Jackson, S.E., van Achterbergh, E., O'Reilly, S. Y., Shee, S.R., 2000. The Hf isotope composition of cratonic mantle: LA-MC-ICPMS analysis of zircon megacrysts in kimberlites. Geochim. Cosmochim. Acta 64, 133–147.

Griffin, W.L., Wang, X., Jackson, S.E., Pearson, N.J., O'Reilly, S.Y., Xu, X.S., Zhou, X.M., 2002. Zircon chemistry and magma mixing, SE China: in-situ analysis of Hf isotopes, Tonglu and Pingtan igneous complexes. Lithos 61, 237–269.

He, J., Wang, B., Wang, L., Wang, Q., Yan, G., 2019. Geochemistry and geochronology of the Late Cretaceous Tongchanggou Mo–Cu deposit, Yidun Terrane, SE Tibet; implications for post-collisional metallogenesis. J. Asian Earth Sci. 172, 308–327.

Henerson, P., 1980. Rare earth element partition between sphene, apatite and other coexisting minerals at the Kangerdlugssuag Intrusion, East Greenland. Contrib. Miner. Petrol. 72, 81–85.

Hou, Z.Q., Qu, X.M., Urabe, T., Takagi, Naito, 2001. Liquid immiscibility of boninite in Xiangcheng, southwestern China, and its implication to genetic relationship between boninite and komatiitic basalt. Acta Geol. Sin.-Engl. 75, 74–93.

Hou, Z.Q., Yang, Y.Q., Wang, H.P., Qu, X.M., Lü, Q.T., Huang, D.H., Wu, X.Z., Yu, J.J., Tang, S.H., Zhao, J.H., 2003. The collisional orogeny and mineralization systems of the Yidun Arc orogen in Sanjiang region, China. Geological Publishing House, Beijing 154–187 (in Chinese with English abstract).

Hou, Z.Q., Qu, X.M., Wang, S.X., Du, A.D., Gao, Y.F., Huang, W., 2004a. Re-Os age for molybdenite from the Gangdese porphyry copper belt on Tibetan Plateau: Implication for geodynamic setting and duration of the Cu mineralization. Sci. China Ser D 47, 221–231.

Hou, Z.-Q., Gao, Y.-F., Qu, X.-M., Rui, Z.-Y., Mo, X.-X., 2004b. Origin of ada- kitic intrusives generated during mid-Miocene east-west extension in southern Tibet. Earth Planet. Sc. Lett. 220 (1-2), 139–155.

Hou, Z.Q., Yang, Y.Q., Qu, X.M., Huang, D.H., Lv, Q.T., Wang, H.P., Yu, J.J., Tang, S.H., 2004c. Tectonic evolution and mineralization systems of the Yidun arc orogen in Sanjiang region, China. Acta. Geol. Sin. 78, 109–120 (in Chinese with English abstract).

Hou, Z., Zaw, K., Pan, G., Mo, X., Xu, Q., Hu, Y., Li, X., 2007. Sanjiang Tethyan metallogenesis in SW China: tectonic setting, metallogenic epochs and deposit types. Ore Geol. Rev. 31 (1-4), 48–87.

Hou, Z., Yang, Z., Qu, X., Meng, X., Li, Z., Beaudoin, G., Rui, Z., Gao, Y., Zaw, K., 2009. The Miocene Gangdese porphyry copper belt generated during post-collisional extension in the Tibetan Orogen. Ore Geol. Rev. 36 (1-3), 25–51.

Hou, Z., Pan, X., Li, Q., Yang, Z., Song, Y., 2013a. The giant Dexing porphyry Cu-Mo-Au deposit in East China: Product of melting of juvenile lower crust in an intracontinental setting. Miner. Deposita 48 (8), 1019–1045.

Hou, Z., Zheng, Y., Yang, Z., Rui, Z., Zhao, Z., Jiang, S., Qu, X., Sun, Q., 2013b. Contribution of mantle components within juvenile lower-crust to collisional zone porphyry Cu systems in Tibet. Miner. Deposita 48 (2), 173–192.

Hou, Z.Q., Yang, Z.M., Lu, Y.J., Kemp, A., Zheng, Y.C., Li, Q.Y., Tang, J.X., Yang, Z.S., Duan, L.F., 2015. A genetic linkage between subduction-and collision-related porphyry Cu deposits in continental collision zones. Geology 43, 247–250.

Hou, Z., Zhou, Y.e., Wang, R., Zheng, Y., He, W., Zhao, M., Evans, N.J., Weinberg, R.F., 2017. Recycling of metal-fertilized lower continental crust: Origin of non-arc Au-rich porphyry deposits at cratonic edges. Geology 45 (6), 563–566.

Hou, Z.Q., Yang, Z.M., Wang, R., Zheng, Y.C., 2020. Further discussion on porphyry Cu-Mo-Au deposits formation in Chinese Mainland. Front Earth Sci-Prc 27, 20–44.

Huang, B., Yan, Y., Piper, J.D.A., Zhang, D., Yi, Z., Yu, S., Zhou, T., 2018. Paleomagnetic constraints on the paleogeography of the East Asian blocks during Late Paleozoic and Early Mesozoic times. Earth-Sci. Rev. 186, 8–36.

Hu, J.M., Meng, Q.R., Shi, Y.R., Qu, H.J., 2005. SHRIMP U-Pb dating of zircons from granitoid bodies in the Songpan-Ganzi terrane and its implications. Acta Petrol. Sin. 21, 867–880.

Jugo, P.J., Luth, R.W., Richards, J.P., 2005. Experimental data on the speciation of sulfur as a function of oxygen fugacity in basaltic melts. Geochim. Cosmochim. Acta 69 (2), 497–503.

Jugo, P.J., 2009. Sulfur content at sulfide saturation in oxidized magmas. Geology 7, 415–418.

Keto, L.S., Jacobsen, S.B., 1987. Nd and Sr isotopic variations of Early Paleozoic oceans. Earth Planet. Sci. Lett. 84 (1), 27–41.

Leng, C.B., Cooke, D.R., Hou, Z.Q., Evans, N.J., Zhang, X.C., Chen, W.T., Danišík, M., McInnes, B.I.A., Yang, J.H., 2018. Quantifying exhumation at the giant Pulang porphyry Cu-Au deposit using U-Pb-He dating. Econ. Geol. 113, 1077-1092.

Li, J.X., Fan, W.M., Zhang, L.Y., Evans, N.J., Sun, Y.L., Ding, L., Guan, Q.Y., Peng, T.P., Cai, F.L., Sein, K., 2019. Geochronology, geochemistry and Sr–Nd–Hf isotopic compositions of Late Cretaceous-Eocene granites in southern Myanmar: Petrogenetic, tectonic and metallogenic implications. Ore Geol. Rev. 112, 103031.

Li, W.C., Zeng, P.Z., Hou, Z.Q., White, N.C., 2011. The Pulang copper deposit and associated felsic intrusions in Yunnan province, Southeast China. Econ. Geol. 106, 79–92.

LI, W., YIN, G., YU, H., LIU, X., 2014. The Yanshanian granites and associated Mo–polymetallic mineralization in the Xiangcheng-Luoji area of the Sanjiang Yangtze conjunction zone in southwest China. Acta. Geol. Sin. (English Edition) 88 (6), 1742–1756.

Li, W.-C., Yu, H.-J., Gao, X., Liu, X.-L., Wang, J.-H., 2017. Review of Mesozoic multiple magmatism and porphyry Cu–Mo (W) mineralization in the Yidun Arc, eastern Tibet Plateau Ore Geol. Rev. 90, 795–812.

Li, Y.-J., Wei, J.-H., Tan, J., Fu, L.-B., Li, H., Ke, K.-J., 2020. Albian-Cenomanian A-type granite-related Ag–Pb–Zn veins in the central Yidun Terrane, SW China: constraints from the Xiasai deposit. Miner. Deposita 55 (6), 1047–1070.

Liu, C., Zhao, G., Liu, F., Shi, J., 2017. Detrital zircon U-Pb and Hf isotopic and whole-rock geochemical study of the Bayan Obo Group, northern margin of the North China Craton: Implications for Rodinia reconstruction. Precambr. Res. 303, 372–391.

Liu, Y., Hu, Z., Gao, S., Günther, D., Xu, J., Gao, C., Chen, H., 2008. In situ analysis of major and trace elements of anhydrous minerals by LA-ICP-MS without applying an internal standard. Chem. Geol. 257 (1-2), 34–43.

Loucks, R.R., 2014. Distinctive composition of copper-ore-forming arc magmas: Aust. J. Earth Sci. 61 (1), 5–16.

Loucks, R.R., Fiorentini, M.L., Henríquez, G.J., 2020. New magmatic oxybarometer using trace elements in zircon. J. Petrol. 61 https://doi.org/10.1093/petrology/egaa034.

Lu, B.X., Wang, Z., 1993. Granitoid and Related Mineralization in the Sanjiang Region. Geological Publishing House, Beijing (in Chinese).

Lu, Y.J., Loucks, R.R., Fiorentini, M.L., Yang, Z.M., Hou, Z.Q., 2015. Fluid flux melting generated post-collisional high-Sr/Y copper-ore-forming water-rich magmas in Tibet. Geology 43, 583–586.

Maniar, P.D., Piccoli, P.M., 1989. Tectonic discrimination of granitoids. Geol. Soc. Am. Bull. 101, 635–643.

Middlemost, E.A.K., 1994. Naming materials in the magma/igneous rock system. Earth Sci. Rev. 37 (3-4), 215–224.

Möller, A., O'Brien, P.J., Kennedy, A., Kröner, A., 2003. Linking growth episodes of zircon and metamorphic textures to zircon chemistry: An example from the ultrahigh-temperature granulites of Rogaland (SW Norway). Geo. Soc. London Special Pub. 220 (1), 65–81.

Mungall, J.E., 2002. Roasting the mantle: Slab melting and the genesis of major Au and Au-rich Cu deposits. Geology 30 (10), 915. https://doi.org/10.1130/0091-7613(2002)030<0915:RTMSMA>2.0.CO;2.

Nardi, L.V.S., Formoso, M.L.L., Müller, I.F., Fontana, E., Jarvis, K., Lamarão, C., 2013. Zircon/rock partition coefficients of REEs, Y, Th, U, Nb, and Ta in granitic rocks: Uses for provenance and mineral exploration purposes. Chem. Geol. 335, 1–7.

Pan, L.-C., Hu, R.-Z., Wang, X.-S., Bi, X.-W., Zhu, J.-J., Li, C., 2016. Apatite trace element and halogen compositions as petrogenetic-metallogenic indicators: Examples from four granite plutons in the Sanjiang region, SW China. Lithos 254-255, 118–130.

Pan, L.-C., Hu, R.-Z., Bi, X.-W., Wang, Y., Yan, J., 2020. Evaluating magmatic fertility of Paleo-Tethyan granitoids in eastern Tibet using apatite chemical composition and Nd isotope. Ore Geol. Rev. 127, 103757. https://doi.org/10.1016/j.oregeorev.2020.103757.

Parat, F., Holtz, F., Klügel, A., 2011. S-rich apatite-hosted glass inclusions in xenoliths from La Palma: Constraints on the volatile partitioning in evolved alkaline magmas. Contrib. Miner. Petrol. 162 (3), 463–478.

Pearce, J.A., 1996. Sources and settings of granitic rocks Episodes 19, 120–125.

Piccoli, P.M., Candela, P.A., 2002. Apatite in igneous systems. Rev. Mineral. Geochem. 48 (1), 255–292.

Qi, L., Hu, J., Gregoire, D.C., 2000. Determination of trace elements in granites by inductively coupled plasma mass spectrometry. Talanta 51, 507–513.

Qu, X.M., Hou, Z.Q., Zhou, S.G., 2002. Geochemical and Nd, Sr isotopic study of the postorogenic granites in the Yidun arc belt of northern Sanjiang region, southwestern China. Resour. Geol. 52, 163–172.

Reid, A.J., Wilson, C.J.L., Phillips, D., Liu, S., 2005. Mesozoic cooling across the Yidun arc, central-eastern Tibetan Plateau: a reconnaissance $^{40}Ar/^{39}Ar$ study. Tectonophysics 398 (1-2), 45–66.

Rempel, K.U., Migdisov, A.A., Williams-Jones, A.E., 2006. The solubility and speciation of molybdenum in water vapor at elevated temperatures and pressures: Implication for ore genesis. Geochim. Cosmochim. Acta 70, 687–696.

Richards, J.P., 1990. Petrology and geochemistry of alkalic intrusives at the Porgera gold deposit, Papua New Guinea. Journal of Geochemical Exploration. J. Geochem. Explor. 35 (1-3), 141–199.

Richards, J.P., 2003. Tectono-magmatic precursorns for porphyry Cu-(Mo-Au) deposit formation. Econ. Geol. 98, 1515–1533.

Richards, J.P., Kerrich, R., 2007. Special paper: Adakite-like rocks: Their diverse origins and questionable role in metallogenesis. Econ. Geol. 102, 537–576.

Richards, J.P., 2009. Postsubduction porphyry Cu-Au and epithermal Au deposits: Products of remelting of subduction-modified lithosphere. Geology 37, 247–250.

Richards, J.P., 2011. High Sr/Y arc magmas and porphyry Cu ± Mo ± Au deposits: Just add water: Econ. Geol. 106, 1075–1081.

Richards, J.P., 2015. The oxidation state, and sulfur and Cu contents of arc magmas: implications for metallogeny. Lithos 233, 27–45.

Roger, F., Jolivet, M., Malavieille, J., 2008. Tectonic evolution of the Triassic fold belts of Tibet. C.R. Geosci. 340, 180–189.

Roger, F., Jolivet, M., Malavieille, J., 2010. The tectonic evolution of the Songpan-Garz (North Tibet) and adjacent areas from Proterozoic to present: a synthesis. J. Asian Earth Sci. 39, 254–269.

Scherer, E., Münker, C., Mezger, K., 2001. Calibration of the lutetium–hafnium clock. Science 293, 683–687.

Sillitoe, R.H., 2010. Porphyry Copper systems. Econ. Geol. 105, 3–41.

Song, X.Y., Zhou, M.F., Cao, Z.M., Robinson, P.T., 2004. Late Permian rifting of the South China Craton caused by the Emeishan mantle plume? J. Geol. Soc. London 161, 773–781.

Sun, W.D., Liang, H.Y., Ling, M.X., Zhan, M.Z., Ding, X., Zhang, H., Yang, X.Y., Li, Y.L., Ireland, T.R., Wei, Q.R., Fan, W.M., 2013. The link between reduced porphyry copper deposits and oxidized magmas. Geochim. Cosmochim. Acta 103, 263–275.

Sun, W.D., Huang, R.F., Li, H., Hu, Y.B., Zhang, C.C., Sun, S.J., Zhang, L.P., Ding, X., Li, C.Y., Zartman, R.E., Ling, M.X., 2015. Porphyry deposits and oxidized magmas. Ore Geol. Rev. 65, 97–131.

Tang, Y.W., Cui, K., Zheng, Z.,Gao, J.F.,M Han, J.J.,Yang, J.H., Liu, L., 2020. LA-ICP-MS Usingle bondPb geochronology of wolframite by combining NIST series and common lead-bearing MTM as the primary reference material:Implications for metallogenesis of South China. Gondwana Res. 83, 217–231.

Wang, D.Z., Hu, R.Z., Hollings, P., Bi, X.W., Zhong, H., Pan, L.C., Leng, C.B., Huang, M.L., Zhu, J.J., 2021. Remelting of a Neoproterozoic arc root: origin of the Pulang and Songnuo porphyry Cu deposits, Southwest China. Miner. Deposita. doi: 10.1007/s00126-021-01049-0.

Wang, R., Richards, J.P., Hou, Z.Q., Yang, Z.M., DuFrane, S.A., 2014a. Increased magmatic water content: The Key to Oligo-Miocene porphyry Cu - Mo ± Au formation in the eastern Gangdese belt. Tibet. Econ. Geol. 109, 1315–1339.

Wang, R., Weinberg, R.F., Collins, W.J., Richards, J.P., Zhu, D.C., 2018a. Origin of postcollisional magmas and formation of porphyry Cu deposits in southern Tibet. Earth-Sci. Rev. 181, 122–143.

Wang, P., Dong, G.C., Zhao, G.C., Han, Y.G., Li, Y.P., 2018b. Petrogenesis of the Pulang porphyry complex, southwestern China: Implications for porphyry copper metallogenesis and subduction of the Paleo-Tethys Oceanic lithosphere. Lithos 304–307, 280–297.

Wang, X.S., Bi, X.W., Leng, C.B., Zhong, H., Tang, H.F., Chen, Y.W., Yin, G.H., Huang, D. Z., Zhou, M.F., 2014b. Geochronology and geochemistry of Late Cretaceous igneous intrusions and Mo-Cu-(W) mineralization in the southern Yidun arc, SW China: implications for metallogenesis and geodynamic setting. Ore Geol. Rev. 61, 73–95.

Wang, X.S., Hu, R.Z., Bi, X.W., Leng, C.B., Pan, L.C., Zhu, J.J., Chen, Y.W., 2014c. Petrogenesisof late Cretaceous I-type granites in the southern Yidun terrane: new constraints onthe Late Mesozoic tectonic evolution of the eastern Tibetan Plateau. Lithos 208–209, 202–219.

Wang, X.S., Williams-Jones, A.E., Bi, X.W., Hu, R.Z., Xiao, J.F., Huang, M.L., 2019. Late Cretaceous Transtension in the Eastern Tibetan Plateau: Evidence From Postcollisional A-Type Granite and Syenite in the Changdu Area. China. J. Geophys. Res-Sol. Ea. 124, 6409–6427.

Whalen, J.B., Currie, K.L., Chappell, B.W., 1987. A-type granites: geochemical characteristics, discrimination and petrogenesis. Contrib. Miner. Petrol. 95, 407–419.

Wu, F.Y., Sun, D.Y., Li, H.M., Jahn, B.M., Wilde, S., 2002. A-type granites in northeastern China: age and geochemical constraints on their petrogenesis. Chem. Geol. 187, 143–173.

Wu, F.Y., Liu, X.C., Ji, W.Q., Wang, J.M., Yang, L., 2017a. Highly fractionated granites: Recognition and research. Sci. China: Earth Sci. 60, 1201–1219.

Wu, T., Xiao, L., Gao, R., Yang, H.J., Yang, G., 2014. Petrogenesis and tectonic setting of the Queershan composite granitic pluton, Eastern Tibetan Plateau: Constraints from geochronology, geochemistry and Hf isotope data. Sci. China: Earth Sci. 44, 1791–1806 (in Chinese with English abstract).

Wu, T., Xiao, L., Wilde, S.A., Ma, C.Q., Zhou, J.X., 2017b. A mixed source for the Late Triassic Garzê-Daocheng granitic belt and its implications for the tectonic evolution of the Yidun arc belt, eastern Tibetan Plateau. Lithos 288–289, 214–230.

Xiao, L., He, Q., Pirajno, F., Ni, P.Z., Du, J.X., Wei, Q.R., 2008. Possible correlation between a mantle plume and the evolution of Paleo-Tethys Jinshajiang Ocean: evidence from a volcanic rifted margin in the Xiaru-Tuoding area, Yunnan, SW China. Lithos 100, 112–126.

Yan, Y., Zhao, Q., Zhang, Y., Huang, B., Zheng, W., Zhang, P., 2019. Direct paleomagnetic constraint on the closure of Paleo-Tethys and its implications for linking the Tibetan and Southeast Asian Blocks. Geophys. Res. Lett. 46, 14368–14376.

Yang, F.C., Li, W.C., Jiang, X.J., Li, C., Wang, Z.Q., Sun, H.Y., Zhou, J.X., 2020. Late Cretaceous granitic intrusions and associated deposits in the Yidun Arc of the eastern Tibetan Plateau. J. Asian Earth Sci. 192, 104249.

Yang, L.Q., Gao, X., He, W.Y., 2015. Late Cretaceous porphyry metallogenic system of the Yidun arc. SW China. Acta Petrol. Sin. 31, 3155–3170 (in Chinese with English abstract).

Yang, L.Q., Deng, J., Dilek, Y., Meng, J.Y., Gao, X., Santosh, M., Wang, D., Yan, H., 2016. Melt source and evolution of I-type granitoids in the SE Tibetan Plateau: Late Cretaceous magmatism and mineralization driven by collision-induced transtensional tectonics. Lithos 245, 258–273.

Yang, Y.H., Zhang, H.F., Xie, L.W., Wu, F.Y., 2007. Accurate measurement of neodymium isotopic composition using Neptune multiple collector inductively coupled plasma mass spectrometry. Chinese J. Anal. Chem. 35, 71–74.

Yang, Z., Yang, L.Q., He, W.Y., Gao, X., Liu, X.D., Bao, X.S., Lu, Y.G., 2017. Control of magmatic oxidation state in intracontinental porphyry mineralization: A case from Cu (Mo–Au) deposits in the Jinshajiang-Red River metallogenic belt. SW China. Ore Geol. Rev. 90, 827–846.

Yin, M.H., 2018. Geochemistry and uranium metallogenic condition of granite rocks of the Haizishan-Genei Area in western Sichuan (MA.Sc Thesis). Chengdu University of Technology, (In Chinese).

Zhao, Y.J., Yuan, C., Zhou, M.F., Yan, D.P., Long, X.P., Cai, K.D., 2007. Post-orogenic extension of Songpan-Garzê orogen in Early Jurassic: constraints from Niuxingou monzodiorite and Siguniangshan A-type granite of western Sichuan, China. Geochemica 36, 139–142 (in Chinese with English abstract).

Zhang, C.C., Sun, W.D., Wang, J.T., Zhang, L.P., Sun, S.J., Wu, K., 2017. Oxygen fugacity and porphyry mineralization: A zircon perspective of Dexing porphyry Cu deposit. China. Geochim. Cosmochim. Acta 206, 343–363.

Zhang, X.F., Li, W.C., Wang, R., Zhang, L., Qiu, K.F., Wang, Y.Q., 2021. Preservation of Xiuwacu W-Mo deposit and its constraint on the uplifting history of Eastern Tibetan Plateau. Ore Geol. Rev. 132, 103995.

Zhou, T., Qi, L., Fan, H.F., Yin, R.S., 2020. An optimized protocol for high precision measurement of 87Sr/86Sr using a Neptune Plus multi-collector inductively coupled plasma mass spectrometer: evaluation of different cone combinations for Sr isotope determination. Anal. Methods 12, 4089–4096.

Zhu, J.J., Richards, J.P., Rees, C., Creaser, R., DuFrane, A., Locock, A., Petrus, J.A., Lang, J., 2018a. Elevated magmatic sulfur and chlorine contents in ore-forming magmas at the Red Chris porphyry Cu-Au deposit, Northern British Columbia. Canada. Econ. Geol. 113, 1047–1075.

Zhu, R.Z., Lai, S.C., Qin, J.F., Zhao, S.W., Santosh, M., 2018b. Strongly peraluminous fractionated S-type granites in the Baoshan Block, SW China: Implications for two-stage melting of fertile continental materials following the closure of Bangong-Nujiang Tethys. Lithos 316–317, 178–198.